October 2021

# ADVANCED MATERIALS DESIGN USING APPLICATION-BASED PROCESSING TECHNIQUES

Daniel S. Camarda
*University of Massachusetts Amherst*

# ADVANCED MATERIALS DESIGN USING APPLICATION-BASED PROCESSING TECHNIQUES

A Dissertation Presented

by

DANIEL SCOTT CAMARDA

Submitted to the Graduate School of the

University of Massachusetts Amherst in partial fulfillment

of the requirements for the degree of

DOCTOR OF PHILOSOPHY

September 2021

Polymer Science and Engineering

**ADVANCED MATERIALS DESIGN USING APPLICATION-BASED PROCESSING TECHNIQUES**

A Dissertation Presented

by

DANIEL SCOTT CAMARDA

Approved as to style and content by:

_____
Alan J. Lesser, Chair

_____
E. Bryan Coughlin, Member

_____
Yanfei Xu, Member

_____
David Hoagland, Department Head
Polymer Science and Engineering

## DEDICATION

*To Nick, Mom, and Dad.*

## ACKNOWLEDGEMENTS

I would like to express my gratitude to Professor Alan J. Lesser for his invaluable support and mentorship throughout the duration of my studies. He passed on a problem-solving mindset that was critical for the completion of the work in this dissertation. I would also like to thank my committee members, Bryan Coughlin and Yanfei Xu for their time, input, and encouragement throughout my graduation milestones.

This work would not be possible without the funding sources: BASF, Rogers Corporation, and CUMIRP. Also, I would like to thank my BASF collaborators, Philippe Desbois, Klaus Stoll, Clause Gabriel, Anna Muller-Cristadoro, Bernhard von Vacano, and Rupert Konradi for their insightful and detailed feedback which guided my progression during multiple projects.

My gratitude extends to group members who served as mentors over the years: Connor Evans, Matt Lampe, Nihal Kanbargi, Madhura Pawar, Arifur Rahman, Brendan Ondra, and Amy Niu. I am also appreciative of my classmates, Chinmay Saraf and Liz Stubbs, who I was fortunate to have in the group with me. I would also like to thank my 2016 entering classmates for comradery while struggling through classes and cumulative exams.

Thank you to the Conte staff members: Lisa Groth, Jessica Skrocki, Cheryl Kehoe, Alyssa Kristek, Maria Farrington, Lisa McNamara, Andre Mel'cuk, Jim, Madelyne Golec, Louis Raboin, Alexander Ribbe, and Weiguo Hu for keeping everything in the department, from logistics to instrumentation, running smoothly.

I was fortunate to be guided by amazing mentors during my undergraduate studies. I would not have pursued graduate school had it not been for the overwhelming encouragement from my undergraduate research advisor, Hugo Caram and Co-Op advisor, Caroline Laufer. Working with them was my gateway into the world of research.

I would also like to thank my amazing friends that I have met in Amherst: Josh Enokida, Marcus Cole, Huyen Vu, James Pagaduan, Hazel Davis, Steve Rosa, Evon Petek, Ryan Selhorst, David Limberg, Liz Stubbs, Christian Steinmetz, Marcel Brown, Robert Enright, Cindy Bukowski, Chrisitan Morneau, Sravya Malempati, Vijesh Tanna, and so many others. Some of the bonds and memories we have shared will last a lifetime. Also, thank you to the Amherst/Northampton Latin Dance community for further enriching my life outside of the lab.

I am grateful to all my friends that I have met at Lehigh (too many to list). Meeting for New Year's and Independence Day has been the breath of fresh air that I have needed every year. Additionally, I would not have gotten through my undergraduate studies without my classmates and study group: Marcus Pugliese, Wesley Michaels, Michaela Gallucci, and Paige Elliott. Further, I am thankful for my childhood friends, Mike and Evan, who maintain contact with me to this day.

Finally, none of this would have been possible without the amazing support from my family: Nick, Mom, and Dad.

## ABSTRACT

### ADVANCED MATERIALS DESIGN USING APPLICATION-BASED PROCESSING TECHNIQUES

SEPTEMBER 2021

DANIEL S. CAMARDA, B.S., LEHIGH UNIVERSITY

M.S., UNIVERSITY OF MASSACHUSETTS AMHERST

Ph.D., UNIVERSITY OF MASSACHUSETTS AMHERST

Directed by: Professor Alan J. Lesser

This dissertation pertains to generating advanced materials using application-based processing techniques. First, billets consisting of PTFE sintering powders are evaluated using Thermomechancal Analysis. It was found that both shape change and volume change are associated with enthalpic and entropic recoil, respectively. These phenomena, due to melting and stored energy during the powder compaction process, were found to be molecular weight dependent. Additionally, kinetics of the recovery and sintering process were found to be slower in blended specimens than pure samples. Next, the creation of graft copolymers by selectively grafting a second polymer to the amorphous fraction of a semi-crystalline polymer in supercritical $CO_2$ is demonstrated. Grafting yields showed an increasing dependence on the polarity of the semi-crystalline polymer used. Upon further characterization of polystyrene-polyamide 6 copolymers, property enhancements such as high glass transition temperatures and the ability to be remelted are elucidated.

Additionally, hydrophobicity is tailored by varying polystyrene composition as well as the grafting polymer. Finally, the use of frontally polymerizable epoxide formulations as adhesives is shown. Lap shear and wire pull-out testing demonstrated adhesion to a wide class of materials, including various polymers, metals, and plywood. Boundary conditions and material properties were shown to significantly affect curing behavior and adhesion results, giving rise to various adhesion mechanisms. Additionally, it has been shown that additives can be used to modify the viscosity of the resin and control volatile formation without negatively impacting the adhesion results.

## TABLE OF CONTENTS

## LIST OF TABLES

## LIST OF FIGURES

# CHAPTER 1

## INTRODUCTION

This dissertation pertains to generating advanced materials using application-based processing techniques. In each chapter, structure-process-property relationships which are relevant to industrial challenges are studied. First, an evaluation of PTFE sintering will be presented. Commercially, this is a time-consuming process which takes place on the order of days. Thus, large quantities of sintering powder must be used for a profit margin to be obtained. Due to the irreversible change in the PTFE crystalline structure upon heat treatment, defective materials cannot be re-sintered. Failed parts, which are inevitably generated, thus account for significant financial detriments. Although this process has been commercialized for decades, investigations regarding the effect of process parameters on final properties of sintered PTFE parts have not been reported. This study will investigate the effect of molecular weight on sintering behavior and properties of PTFE. This includes the extent of shape change and volume change that occurs during specific regions of the sintering profile as well as recovery and densification kinetics. Mechanical and thermal properties of sintered billets will also be presented.

Next, studies focusing on fabricating graft copolymers using supercritical $CO_2$ for polymer upcycling will be discussed. Supercritical $CO_2$ is a green solvent that allows for rapid transport of small molecules in polymeric matrices. Due to size exclusion, penetration only occurs within the amorphous regions of semi-crystalline polymers. Thus, grafting is facilitated by transporting monomer and free radical initiator within amorphous regions

such that covalent bonding occurs selectively to amorphous regions during polymerizations. This provides a cost-effective, sustainable method for upcycling semi-crystalline polymeric waste. Grafting is performed on three semi-crystalline polymers: polyamide 6 (PA6), polyethylene terephthalate (PET), and isotactic polypropylene (iPP). Characterization of each polymer as well as the grafting yield is presented. The influence of the semi-crystalline polymer on the graft yield is discussed herein. Following this, PA6 graft copolymers are further characterized to assess thermal properties, moisture resistance, and grafting molecular weight. Additionally, di(ethylene glycol) methyl ether methacrylate is polymerized within PA6 using the same grafting procedure and swelling experiments are performed to assess whether hydrophilicity can be achieved in contrast to the hydrophobic grafted polystyrene (PS). Thus, potential added value to this widely used engineering plastic from the grafting process is assessed and discussed herein.

Finally, adhesion mechanisms of frontally polymerized epoxide formulations will be presented. Frontal polymerization (FP) is a self-propagating reaction which generates a spatially propagating, localized reaction zone. Fronts of this nature are self-sufficient to polymerize following point initiation without the use of additional external energy. Although FP is particularly advantageous for adhesives by providing the ability to be cured on demand, heat loss from the reaction to the surroundings becomes a limiting factor in achieving full front propagation. Accordingly, the scope of FP adhesive applicability has been limited to a small range of materials and configurations. Herein, we present an epoxy formulation that undergoes FP effectively through buried interfaces and provides adhesion to a broad class of materials. Lap shear and wire pull-out testing are performed to determine

the adhesive strength. The effect of boundary conditions on curing and adhesion results will be presented. In the context of these findings, the mechanisms of adhesion to various substrates are also elucidated.

# CHAPTER 2

# THE EFFECT OF MOLECULAR WEIGHT ON THE STRUCTURAL RECOVERY AND SINTERING BEHAVIOR OF PTFE

## 2.1 Introduction

Polytetrafluoroethylene (PTFE) is a fluoropolymer with high chemical resistance, moisture resistance, thermal stability, electrical insulation, biocompatibility, and low coefficient of friction. Due to these favorable properties, PTFE has been used in a wide range of applications such as aeronautical components, surgical implants, containers for corrosive liquids, wire coatings, components for electrical devices, high stretch tapes, and others.[1–7]

Ultra-High Molecular Weight Polytetrafluoroethylene (UHMWPTFE), due to its high melt viscosity ($10^{10}$-$10^{11}$ poise) cannot be processed using conventional techniques such as extrusion or injection molding.[8] Thus, commercial processing of PTFE first involves forming a green billet from granular or fine powder, followed by sintering at a temperature above the melting point (typically in the range of 370°C). Finally, cooling is employed to crystallize the molten PTFE before machining.[9] The billet formation procedure can vary depending on the application. In some cases, billets are formed by compacting powder into a mold and applying a preform pressure. For applications such as piping and wire, which require longer lengths of material, a semi-continuous process such as paste extrusion is used. The steps are outlined in the schematic in Figure 1.[3]

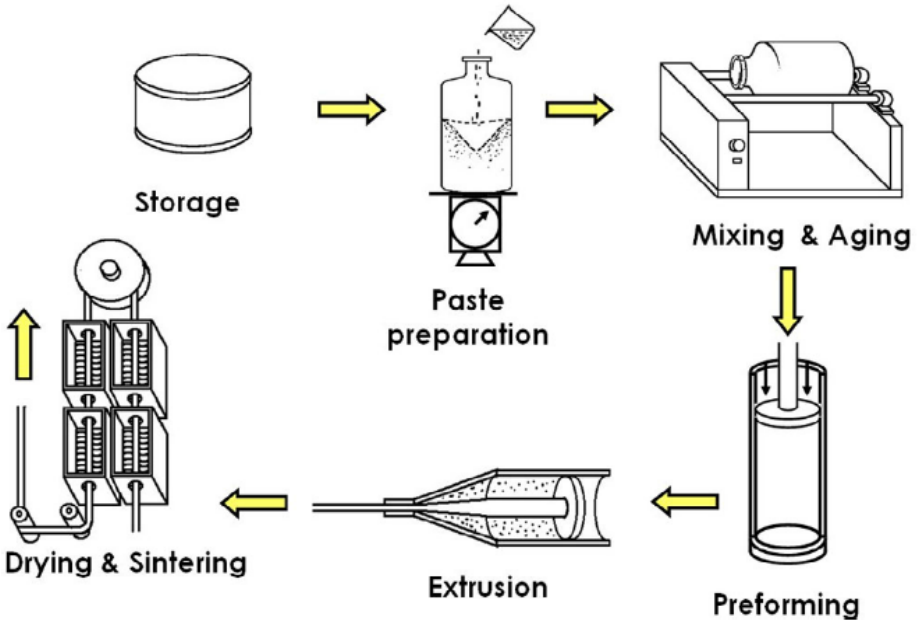


**Figure 1:** Schematic of the paste extrusion process (figure taken from reference 3).

First, the powder is mixed with a lubricant such that it can be introduced into the extruder. Continuous mixing is then applied to form a homogenous paste. Next, a low preforming pressure is applied to minimize voids before extrusion. Following the extrusion process, extrudate is then placed into a drier where the lubricant is evaporated, followed by sintering above the melting point. No matter the process, each step is crucial in engineering a final part with mechanical integrity. Preforming pressure, sintering temperature, sintering time, cooling rate, etc. are important parameters to tune when optimizing the PTFE sintering process. However, studies to generate an understanding of these process variables on PTFE properties have not been reported in literature.

The first attempt to model sintering was implemented by Frenkel in 1945.[10] From a purely Newtonian perspective, the model states that sintering is driven by surface tension

and viscosity of the coalescing particles. Though outdated, this model remains the most accepted universal description for sintering.[11] Many aspects of polymer flow, however, are not accounted for, leaving the phenomena of polymer sintering poorly understood.[12] In fact, studies regarding sintering of UHMWPTFE, given its extremely high melt viscosity and low surface tension, contradicts Frenkel's model, demonstrating that sintering is rather driven by entanglement formation from a nearly 100% crystalline state.[13] It should be noted that virgin and sintered PTFE have different crystalline structures. The crystalline structure of virgin PTFE consists of extended chain crystals (ECC) formed due to crystallization during the polymerization process. Once melted, however, the chains fold and recrystallize into folded chain crystals (FCC), where crystallinity and melt temperature drastically drops.[6] This is an irreversible transition and further motivates the need for optimizing sintering of this material as melted powders cannot be recycled.

Due to these concerns, recent studies have focused on what effect preforming pressure has on the sintering behavior and properties of UHMWPTFE. The findings from these studies indicate that the sintering process is anisotropic and with increasing anisotropy occurring on billets formed at higher compaction pressures. Careful investigation of this process also showed that most, if not all, of the shape change that occurs during the sintering process happens early while the billet undergoes an expansion process due to crystal melting and entropic molecular rearrangement.

Overall, four distinct regions were observed when sintering using Thermomechanical Analysis (TMA) on preformed cylindrical billets. These regions were: thermally induced densification that occurs just prior to melting (a), enthalpic structural

recovery during melting (a-b), entropic structural recovery (b-c), and isotropic densification (d). These regions are shown in Figure 2, where ΔH is the change in height and $H_0$ is the initial height. $\Delta H/H_0$ is therefore the engineering strain in the axial direction, defined as the normalized height ratio.

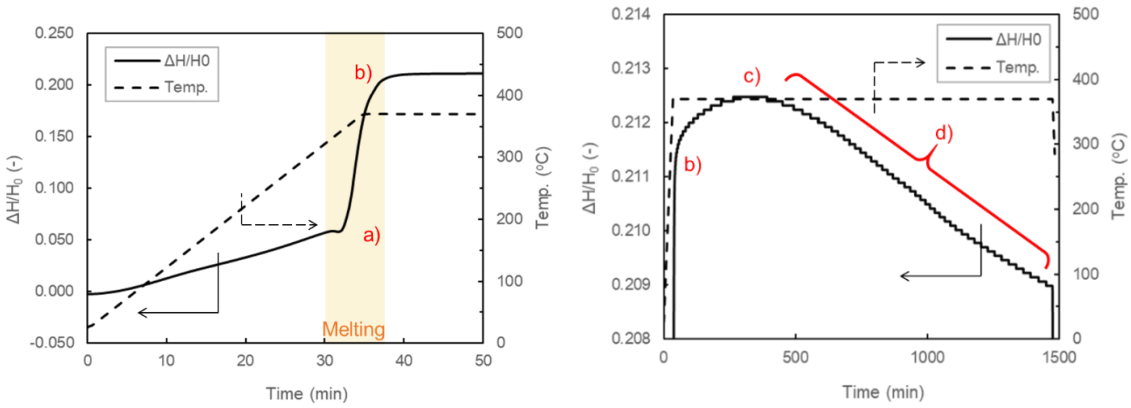


**Figure 2:** Normalized height ratio versus time during melting (left) and normalized height ratio versus time at later stages of sintering (right).

It was found that the densification before melting and overall expansion are pressure dependent. Densification before melting decreases with increasing pressure while overall expansion increases with increasing preform pressure. The increased expansion indicates that more memory is stored in PTFE crystals as higher preforming pressures are applied. Additionally, anisotropy factor ($A_f$), defined by the axial expansion ratio relative to the transverse expansion ratio (equation 2.1), also increases with increasing pressure and is indicative of shape change. These pressure dependent observations are shown in Figure 3.

$$A_f = \frac{Axial\ expansion\ ratio}{Transverse\ expansion\ ratio} = \frac{H(t)/H_0}{D(t)/D_0} \tag{2.1}$$

$A_f$ is the anisotropy factor, H(t) and D(t) is the height and diameter at a given time, t, respectively, and $H_0$ and $D_0$ is the initial height and diameter, respectively. In this case, t is the time at which the sintering process was completed.

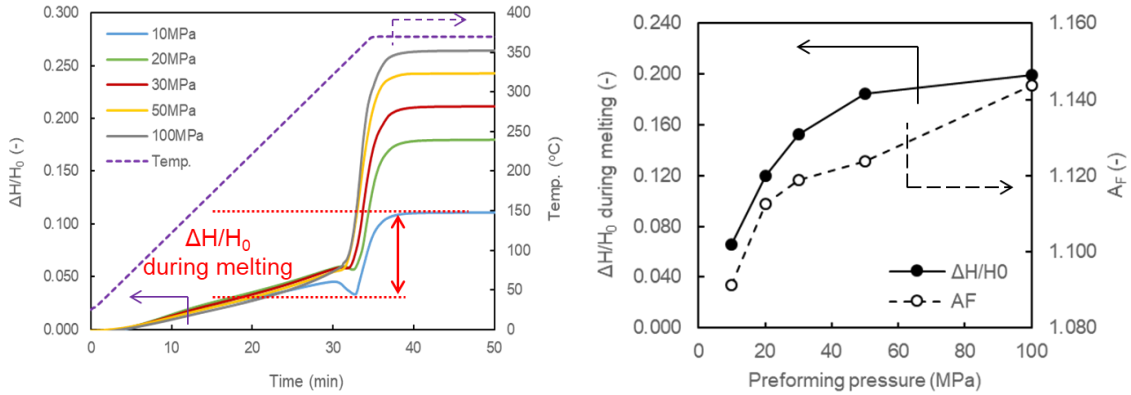


**Figure 3:** Expansion during melting at various preform pressures (left) and anisotropy factor versus preform pressure (right).

As can be seen, the increased anisotropy factor with increasing pressure indicates that more shape change occurs as preforming pressure increases. Separate experiments where samples were quenched at various stages during melting show that all the shape change occurs before region c. This indicates that UHMWPTFE crystals undergo recoil during melting. Additional shape change occurs between regions b-c during the entropic recovery stage. This region occurs over the course of approximately six hours and is associated with molecular recoil due to the preform pressure. Following this, isotropic densification occurs in the melt associated with either entanglement formation or porosity reduction, as expected. During recrystallization, further densification also occurs.

Herein, we investigate the effect of molecular weight on the structural recovery and sintering behavior of PTFE. Granular powders of molecular weights that differ by an order of magnitude as well as blends are compacted to cylindrical green billets. Differential Scanning Calorimetry and X-Ray scattering measurements are performed on nascent powders and green billets to investigate any morphological changes associated with the compaction process. Then, TMA measurements are conducted to study the shape change, volume change, and kinetics associated with various regions of the sintering profile. The measurements elucidate that many of these aspects are molecular weight dependent, with unusual behavior observed in the blend. Finally, compression testing is performed to investigate the mechanical properties of sintered billets.

In contrast to these traditional sintering methods, Selective Laser Sintering (SLS) 3D printing is a more recent, additive manufacturing process by which materials are formed by sintering particles in a layer-by-layer fashion.[14] This allows for complex geometries to be produced without the need for additional tooling to generate parts that do not match the form of processing design constraints.[15] Such additional equipment is costly and adds labor intensity to production with earlier substrative manufacturing methods like traditional sintering, molding, extrusion or blending.[16] Specifically, almost all material used in SLS printers today are polyamides because their low melt viscosity allows for fast sintering. In these cases, sintering occurs when the powder is heated beyond the melt temperature and is thus driven by melting of the crystals.[17] Incorporating a wider range of polymers has been a challenge because many do not exhibit the low viscosity needed to allow for strong sintering characteristics. A possible method to drive sintering is to utilize reciprocal fluxes

by immobilizing powders in a non-equilibrium state. Upon melting, the mobility introduced will allow sintering to be enhanced by the thermodynamic driving force to achieve equilibrium. Many of the methods used in this chapter can be applied to studying non-equilibrium SLS powders. Future opportunities for this work will be discussed in Chapter 5.

## 2.2 Materials and Methods

PTFE granular powder was provided by Rogers Corporation. Two grades used for this study are labeled 60X and 601X, exhibiting molecular weights of 60 and 601 kDa, respectively. An equal part by mass blend was created using these two grades, labeled 50/50. All powders were stored in a freezer at -40°C until use. Optical microscopy was used to obtain images of each nascent powder.

### 2.2.1 Powder Compaction

Powders were compacted into green billets using the following procedure: Approximately 2.56 g of powder was initially placed into a 13 mm diameter cylindrical mold. Compaction was performed using an Instron 5500R Mechanical Tester where a cylindrical insert was pressed through the mold in compression. This was done in three steps: a constant pressure 4 MPa for 5 min was applied for the first two steps, and 30 MPa for 10 minutes was applied for the final step in fabricating each billet. In between each step, more powder was placed in the mold. The total mass of each fabricated billet was approximately 3.56 g. A schematic of the mold as well as the compressive fabrication profile is shown in Figure 4. Following billet fabrication, specimens were stored at room

temperature for three hours before use. It should be noted that four green billets were created for each specimen. Three green billets for each grade were used for sintering studies while the remaining billet was used for DSC and Wide-Angle X-Ray Scattering (WAXS) measurements.

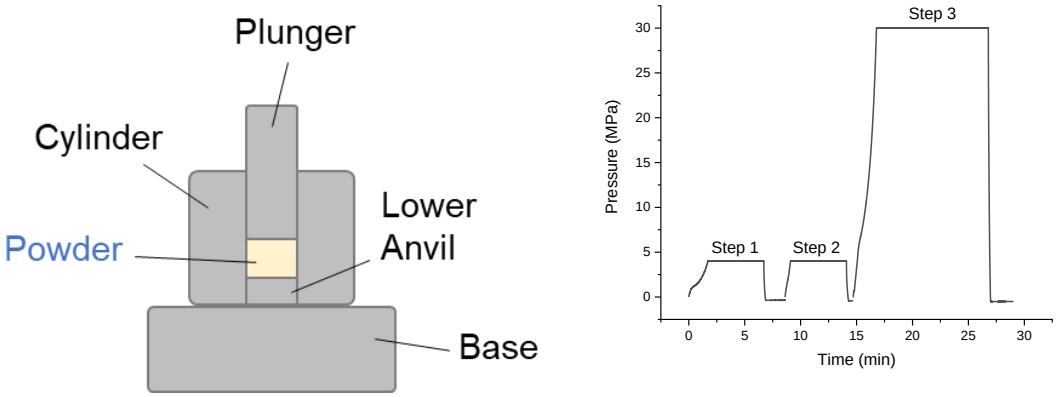


**Figure 4:** Schematic of cylindrical mold (left) and plot of preform pressure profile (right).

### 2.2.2 Thermal Analysis

Thermomechanical Analysis (TMA) was performed on green billets using a TA Instruments TMA model Q400. Three repeat runs of each specimen were conducted. An expansion probe was used with a preload force of 0.1 N and an oscillatory force of 0.02 N at a frequency of 0.5 Hz. Sintering was performed at 370°C for 24 hours with heating and cooling rates of 10 K per minute. A depiction of this setup as well as the sintering profile is shown in Figure 5.

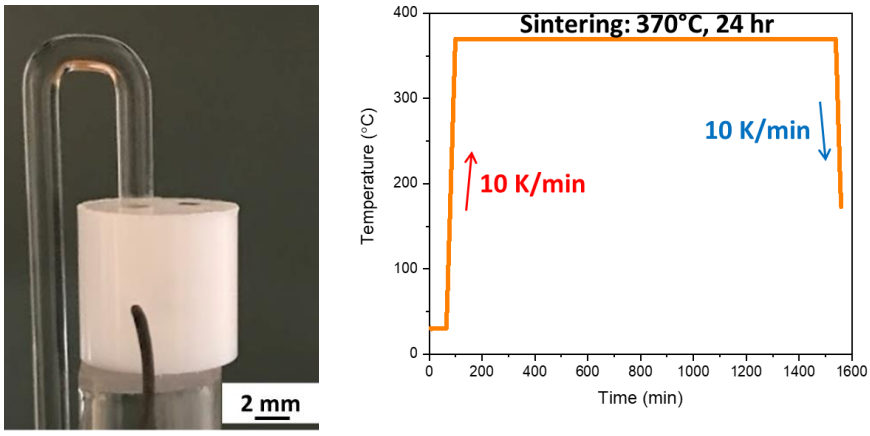


**Figure 5:** TMA setup with expansion probe on billet (left) and sintering profile (right).

Measurements of both green billets and sintered billets were taken, including density, anisotropy factor, and isotropy factor, defined by equation (2.2)

$$I_f = \frac{V(t)}{V_0} \tag{2.2}$$

where $I_f$ is the isotropy factor, V(t) is the volume of the billet at a given time, t, and $V_0$ is the initial volume. For the purposes of this study, both the anisotropy and isotropy factor were measured by comparing dimensions of green billets to dimensions after removal of the billets from the TMA, that is, after the entire sintering process was completed.

Differential scanning calorimetry (DSC) was performed using a TA Instruments Q200 Differential Scanning Calorimeter equipped with RCS90 device for low temperatures. On all specimens, two heating scans were performed with one cooling cycle in between. The temperature range was 0 to 370°C for all specimens. Heating and cooling rates were 10 K/min. This was performed on nascent powders, green and sintered billets.

### 2.2.3 Wide Angle X-Ray Scattering

Wide Angle X-Ray Scattering (WAXS) was conducted using a SAXSLAB Ganesha 300XL next generation SAXS system with CuKα radiation. Each measurement was performed at a q-range of 0.6 – 2.9 Å for 180 s. Spectra were collected for nascent powder, green billets, and sintered billets. The diffraction data was then further analyzed to calculate the crystallinity of sintered billets using the relative areas between the crystalline and amorphous peaks. Additionally, the Scherrer equation was used to calculate crystallite size:[18]

$$L = \frac{K\lambda}{b\cos\theta} \tag{2.3}$$

Where L is the crystallite size, K is a dimensionless shape factor, b is the full width at half maximum (FWHM) of the crystalline diffraction peak, and θ is the crystalline peak Bragg angle.

### 2.2.4 Compression Testing

Compression testing of sintered billets was performed using an Instron 5500R Mechanical Tester. A controlled strain rate of 2 mm/min was applied. Loading and unloading curves were measured for each specimen.

## 2.3 Results and Discussion

### 2.3.1 Characterization of Nascent Powders and Green Billets

Optical images of each nascent are shown in Figure 6.

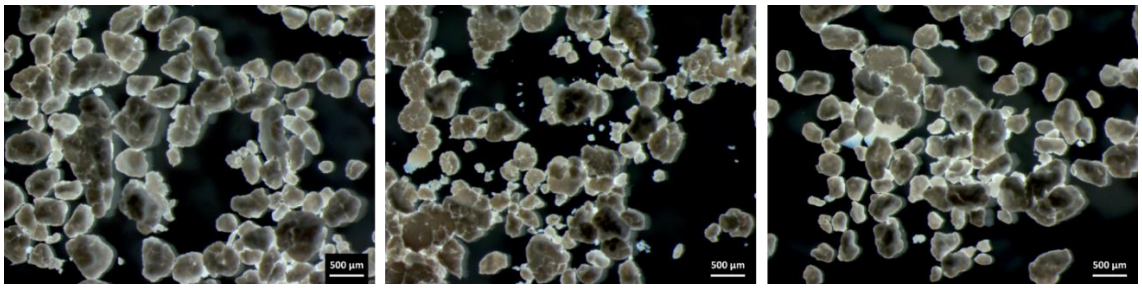


**Figure 6:** Optical images of each powder: 60X (left), 50/50 (middle), and 601X (right).

As can be seen, the morphology of the powders is granular and elliptical, with sizes ranging from 100-500 µm. No obvious morphological differences are apparent between each powder.

DSC traces of each powder are shown in Figure 7. Results are tabulated in Table I.

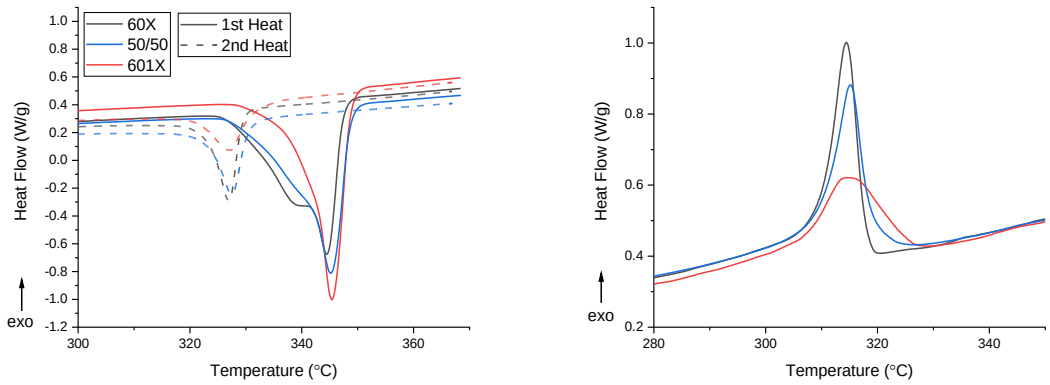


**Figure 7:** DSC traces of nascent powders. Heating and cooling scans are shown on the left and right plots, respectively.

**Table I:** DSC results of nascent powders. $T_m$, $\Delta H_m$, $X_c$, $T_c$, and $\Delta H_c$ are the melt temperature, melting enthalpy, crystallinity, crystallization temperature, and crystallization enthalpy, respectively. 61.1 J/g was used as the enthalpy of a perfect PTFE crystal.[19]

| Specimen | First Heat | | | First Cool | | Second Heat | | |
|---|---|---|---|---|---|---|---|---|
| | $T_m$ (°C) | $\Delta H_m$ (J/g) | $X_c$ (wt %) | $T_c$ (°C) | $\Delta H_c$ (J/g) | $T_m$ (°C) | $\Delta H_m$ (J/g) | $X_c$ (wt %) |
| **60X** | 345 | 66.75 | 109 | 314 | 18.15 | 327 | 18.15 | 30 |
| **50/50** | 345 | 66.54 | 109 | 315 | 20.97 | 327 | 18.33 | 30 |
| **601X** | 345 | 63.15 | 103 | 314 | 17.43 | 327 | 14.51 | 24 |

The measured crystallinity of these powders is above 100 wt %, an overestimation because the melting enthalpy of a perfect PTFE crystal is controversial and reported over a wide range (between 57 and 82 J/g).[2,19–21] Realistically, these PTFE powders exhibit nearly 100 wt % crystallinity due do their ECC structure. On second heating scans, the crystallinity and melt temperatures significantly decrease indicating an FCC structure.

DSC measurements of green billets following the compaction process were also taken. These results are shown in Figure 8 and Table II.

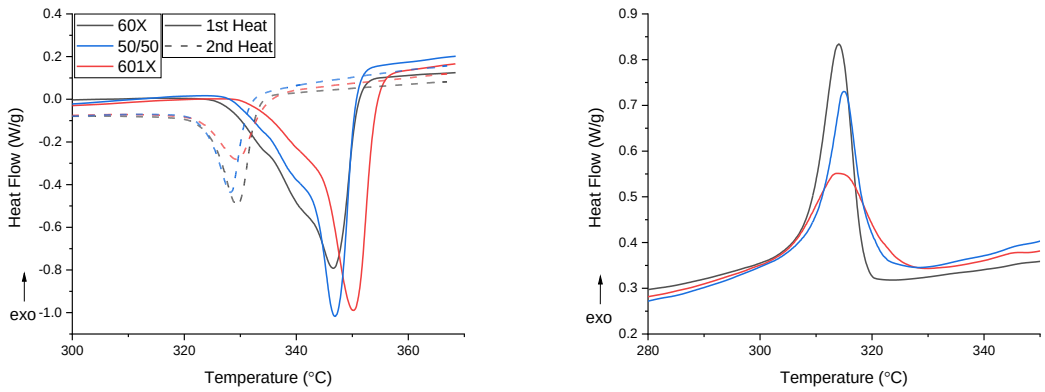


**Figure 8:** DSC traces of green billets. Heating and cooling scans are shown on the left and right plots, respectively.

**Table II:** DSC results of green billets.

| Specimen | First Heat | | | First Cool | | Second Heat | | |
|---|---|---|---|---|---|---|---|---|
| | $T_m$ (°C) | $\Delta H_m$ (J/g) | $X_c$ (wt %) | $T_c$ (°C) | $\Delta H_c$ (J/g) | $T_m$ (°C) | $\Delta H_m$ (J/g) | $X_c$ (wt %) |
| **60X** | 347 | 63.46 | 104 | 314 | 21.54 | 329 | 19.67 | 32 |
| **50/50** | 347 | 62.5 | 102 | 315 | 17.66 | 328 | 14.36 | 23 |
| **601X** | 350 | 60.76 | 99 | 314 | 15.66 | 330 | 13.94 | 23 |

Compared to the nascent powders, melt temperatures have increased slightly. This indicates that lamellar may have thickened due to crystals fusing together during the compaction process. However, all other results are relatively similar to the nascent powders. Thus, any structural changes due to compaction were not significant enough to be demonstrated using this technique. Therefore, WAXS measurements were conducted to elucidate this. Results of nascent powders and green billets are shown in Figure 9 and Table III.

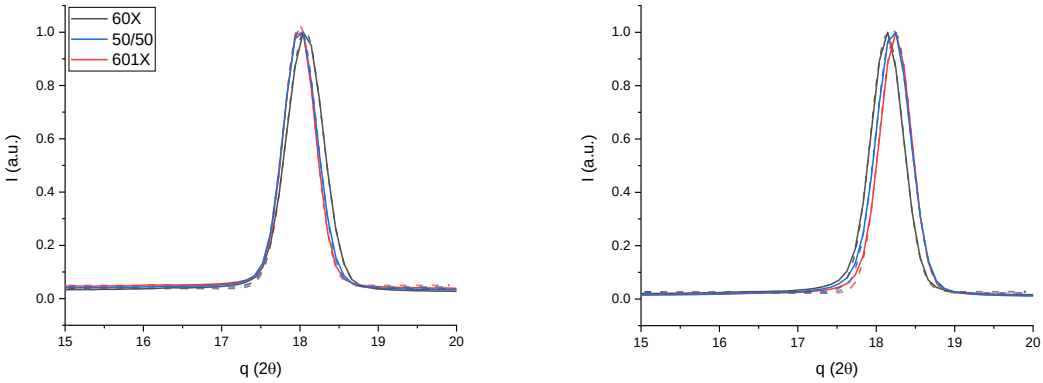


**Figure 9:** WAXS of nascent powder (left) and green billets (right). Curves were fit to gaussian functions as shown by the dashed lines.

**Table III:** WAXS analysis of nascent powder and green billets. The crystallite size was calculated using the Scherrer equation.

| Specimen | Powder | | | Preformed Billet | | |
|---|---|---|---|---|---|---|
| | 2θ (°) | FWHM (°) | Crystallite Size (Å) | 2θ (°) | FWHM (°) | Crystallite Size (Å) |
| **60X** | 18.06 | 0.549 | 163 | 18.14 | 0.495 | 181 |
| **50/50** | 18.00 | 0.509 | 176 | 18.22 | 0.521 | 172 |
| **601X** | 17.99 | 0.478 | 187 | 18.25 | 0.482 | 185 |

The peak at ~18° is indicative of the [100] crystallographic diffraction plane. As expected, no amorphous halo is observed as these specimens are nearly 100% crystalline. The crystallite size increases with molecular weight of the nascent powders. The crystallite size of the preform billets, however, is lower for the blend than pure specimens. Also, the crystallite size appeared to increase in the lower molecular weight specimen due to the compaction process while the others remained unchanged. This is additional evidence, in complement to the increase in melt temperature as observed by DSC, that some structural change may have been imposed due to the compaction process.

### 2.3.2 Sintering Studies

TMA results as a function of temperature are shown in Figure 10.

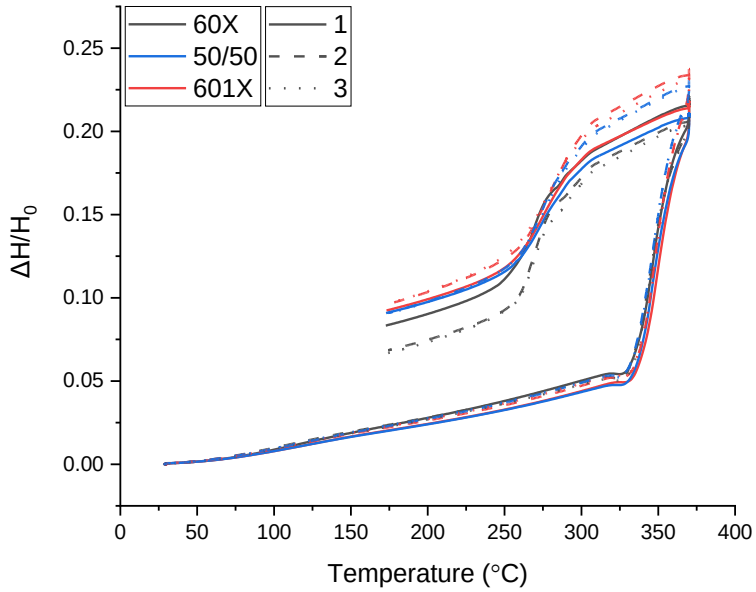


**Figure 10:** Normalized height ratio (axial engineering strain) versus temperature. Three runs for each PTFE grade were performed.

As can be seen, the normalized height ratio measurements are repeatable and finely resolved. Initially for all specimens, an increase in normalized height ratio versus temperature is observed due to thermal expansion. Then, a rapid increase due to melting occurs ranging from 325 - 370°C. During cooling, the normalized height ratio then decreases as crystallization occurs due to densification.

More information can be garnered by viewing the normalized height ratio traces as a function of time. For simplicity, one representative run for each molecular weight specimen was plotted in Figure 11.

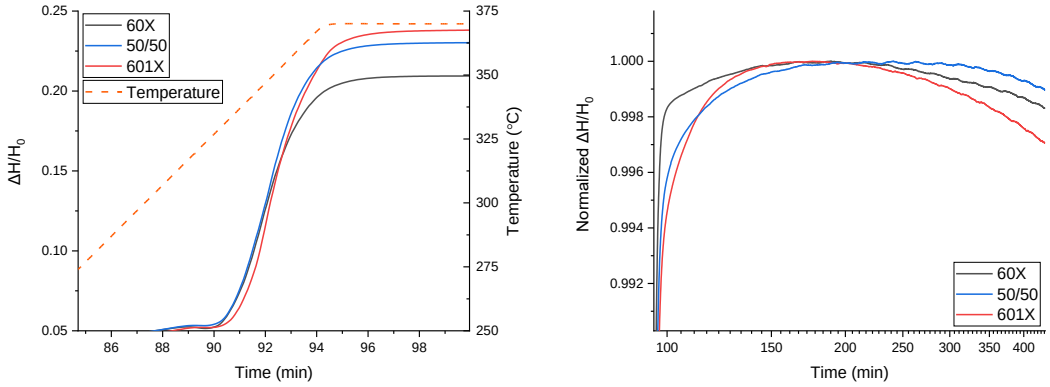


**Figure 11:** Normalized height ratio versus time during melting (left) and normalized height ratio versus time following melting (right). Note: the y-axis of the figure on the right was subjected to a min-max normalization for ease of viewing.

Similar to previous observations when studying the effect of pressure, an initial fast, enthalpic recovery is observed due to melting from 90 – 95 min. Following this, a slower, entropic recovery is observed from 100 – 200 min. This is suspected to arise from recoil due to the anisotropic deformation introduced during the compaction process. Recent studies done by the author's group were where samples were quenched at various stages during this recovery window showed that the anisotropy factor increases until maximum recovery is reached. This indicates that all the anisotropic shape change occurs in both the enthalpic and entropic regions. While a majority of the recovery time takes place in the entropic regime, it can also be seen that less than 1% of the overall expansion occurs in

this region. Conversely, nearly all the recovery occurs in the enthalpic region. The overall maximum expansion as well as the time required to reach peak expansion is quantified in Figure 12.

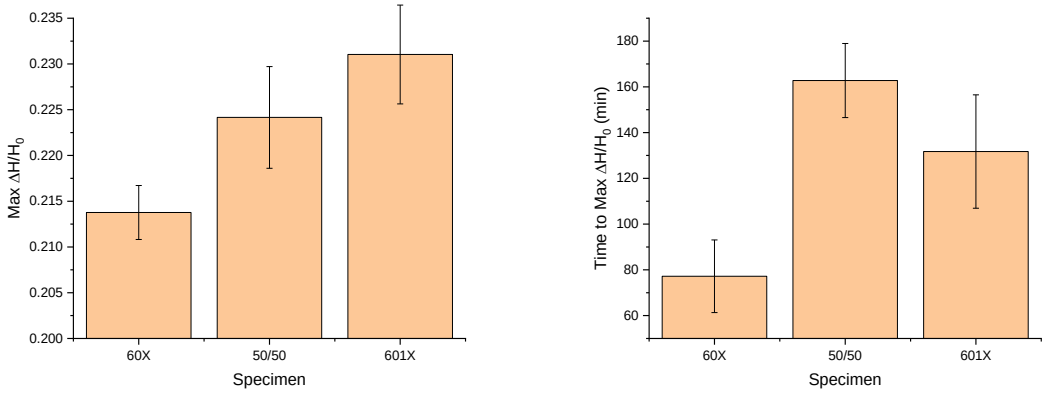


**Figure 12:** Maximum normalized height ratio (left) and recovery time (right) for each molecular weight specimen. Error bars represent three measurements.

As can be seen, the maximum normalized height ratio increases with molecular weight. Because the contribution to the height change is mostly enthalpic, this indicates that more memory is stored in the PTFE crystals during the compaction process as molecular weight increases. Time to reach maximum height, however, is additive with molecular weight for the pure specimens, but slowest for the blend. For the pure specimens, this is expected due to the higher mobility of lower molecular weight chains. The slower kinetics of the blend, however, is interesting and has never been reported previously. A possible explanation of this is that the blend, given its mixture of two drastically contrasting molecular weights, introduces varying magnitudes of anisotropy stored during compaction. Thus, it is plausible that the interfaces between crystals at varying alignments create an additional

barrier to entanglement formation such that isotropy needs to be fully created prior to molecular diffusion.

The anisotropy factor and isotropy factor measurements are shown in Figure 13.

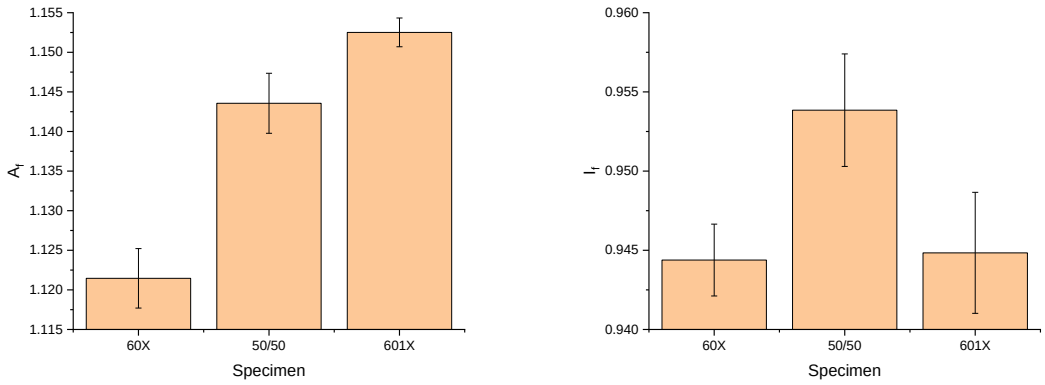


**Figure 13:** Anisotropy factor (left) and isotropy factor (right). Error bars represent three measurements.

As can be seen, anisotropy factor increases with molecular weight. As expected, this follows the same trend as the normalized height ratio, as both are associated with shape change during recovery. This means that more latent free energy is stored in higher molecular weight chains during the compaction process, analogous to previous studies which show that anisotropy factor increases with increasing preforming pressure. The isotropy factor, however, is associated with volume change, and is higher for the blend than the pure specimens.

The isotropic densification regime and densification rate is shown in Figure 14.

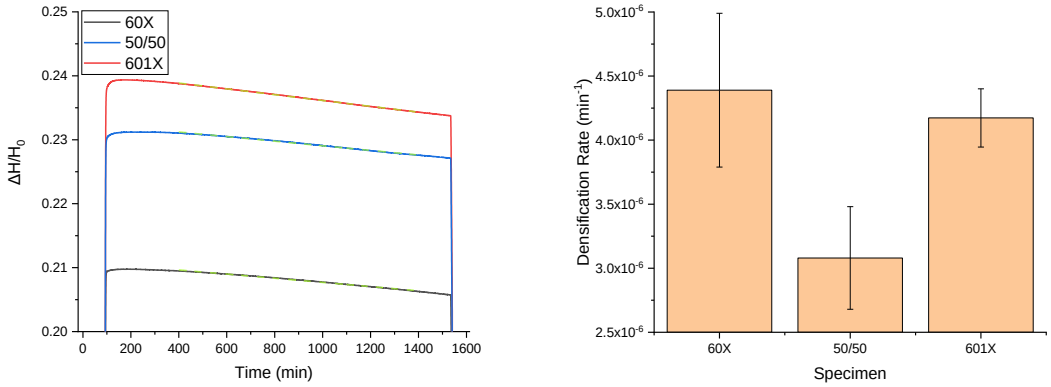


**Figure 14:** Densification during isothermal conditions (left) and densification rate (right). Liner fits were performed from 400 – 1400 min (dashed lines) and slopes were reported as the densification rate. Error bars represent three measurements.

As can be seen, isotropic densification during sintering occurs over the entire sintering window. Regardless of molecular weight, equilibration is not reached within the 24-hr. isothermal timespan, revealing the slow sintering kinetics intrinsic to PTFE. Like the recovery kinetics, densification kinetics are slower for the blend than the pure specimens. If entanglement formation was purely responsible for densification, the trend should be additive with molecular weight. However, it is likely that a combination of porosity reduction, entanglements, and other factors associated with melt memory play a role.

Density and density ratios are shown in Figure 15.

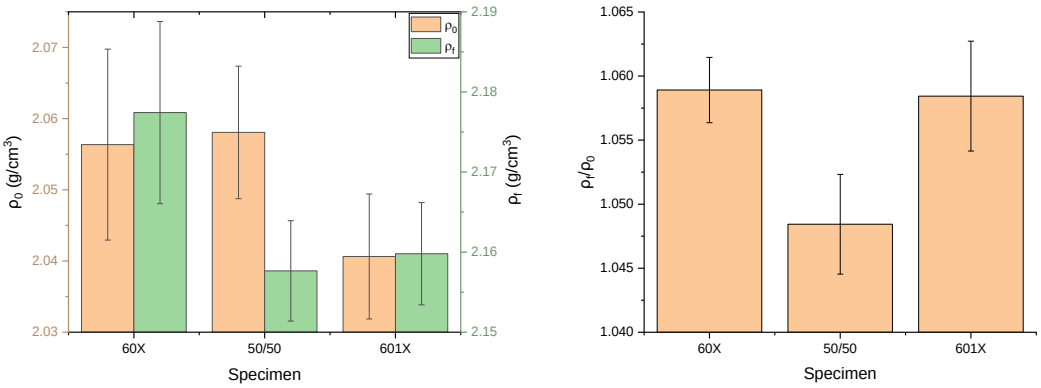


**Figure 15:** Density of green billets, $\rho_0$, and density of sintered billets, $\rho_f$ (left). Density ratios (right). Error bars represent three measurements.

Density values of green billets are statistically similar for each specimen. Although density values of sintered billets show that 60X is higher than the others, the difference is miniscule (less than 1%). Additionally, density ratios show the same trend as densification rate and isotropy factor. This is expected as the faster densification rates of the pure specimens enable more densification during sintering compared to the blend. The isotropy factor is also larger for the blend because less densification occurred during sintering, causing a larger net volumetric expansion. Overall, the specimens densify on the order of 5-6 % during sintering. That is, the density of the green billets is large before any sintering occurs, akin to the deformability of the ECC structure and extremely high level of crystallinity when compared to the sintered billets, where the crystal structure transforms to the FCC structure and degree of crystallinity drops to roughly half of the green billet.

The storage modulus versus temperature as well as storage modulus versus sintering time for each run is shown in Figure 16.

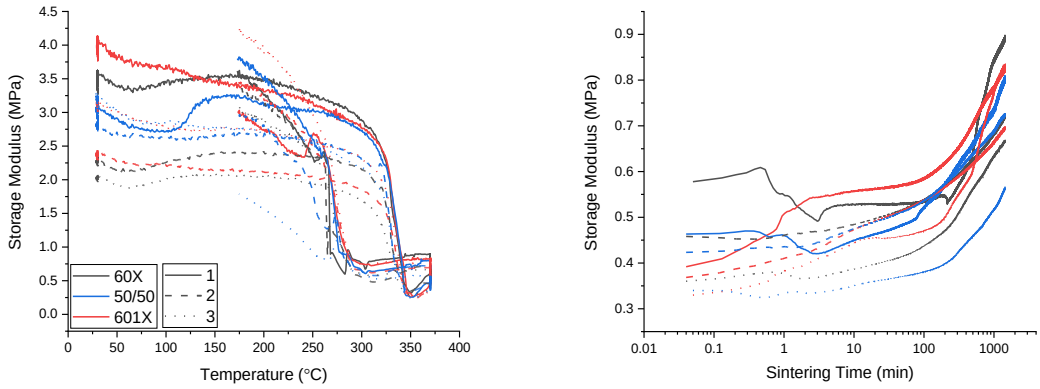


**Figure 16:** Storage Modulus versus temperature (left) and storage modulus versus sintering time (right) during the 24-hr. sintering region at 370°C.

It shows that under these loading conditions, the storage modulus results appear nonrepeatable and relatively irregular. One proposition is that because the contact area between the probe and sample is miniscule, local effects play a large role in the modulus results that are not indicative of the bulk sintering behavior. Additionally, the normal force applied is small such that a resolved sample response could not be achieved. Thus, these data are inconclusive; however, another set of experiments were performed where a Tzero lid was placed in between the probe and billet to increase the contact area of the applied load as shown in Figure 17. Additionally, the preload force was increased to 0.5 N.

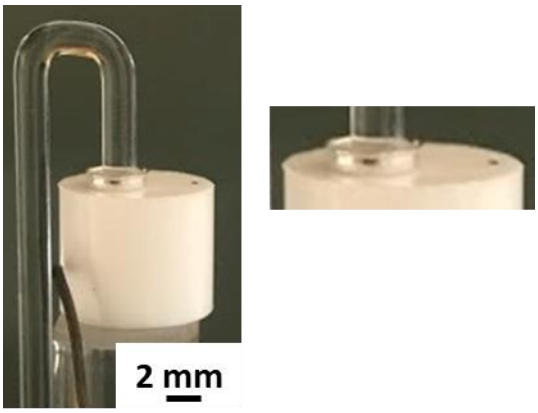


**Figure 17:** Adjusted TMA setup.

The modulus traces from this setup are shown in Figure 18.

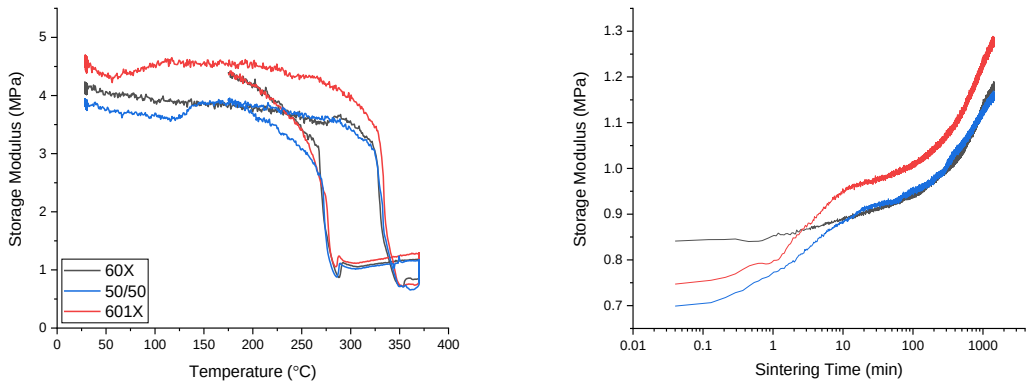


**Figure 18:** Storage Modulus versus temperature (left) and storage modulus versus sintering time (right) during the 24-hr. sintering region at 370°C.

As can be seen, the traces are cleaner as compared to the previous loading conditions. However, the increased normal force caused the probe and lid to sink into the melt, compromising the ability to monitoring of the normalized change in height results. Future

work includes adjusting these parameters such that all data sets can be accurately gathered and interpreted simultaneously.

### 2.3.3 Characterization of Sintered Billets

DSC results of sintered billets are shown in Figure 19 and Table IV.

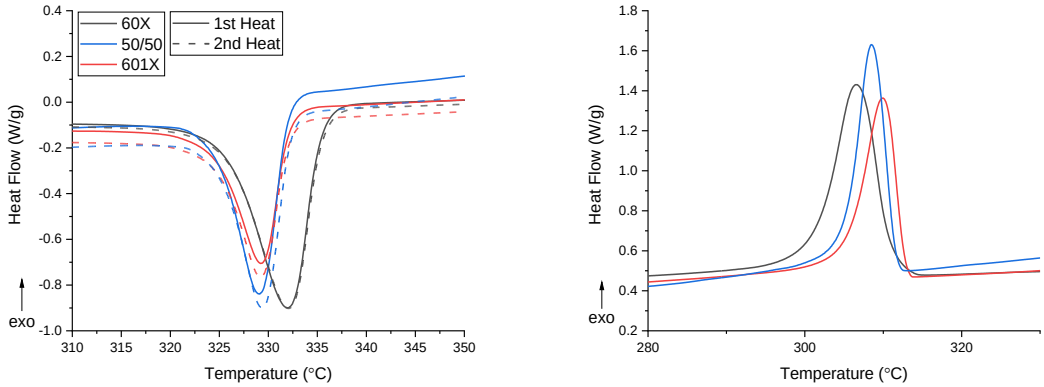


**Figure 19:** DSC traces of sintered billets. Heating and cooling scans are shown on the left and right plots, respectively.

**Table IV:** DSC results of sintered billets.

| Specimen | First Heat | | | First Cool | | Second Heat | | |
|---|---|---|---|---|---|---|---|---|
| | $T_m$ (°C) | $\Delta H_m$ (J/g) | $X_c$ (wt %) | $T_c$ (°C) | $\Delta H_c$ (J/g) | $T_m$ (°C) | $\Delta H_m$ (J/g) | $X_c$ (wt %) |
| **60X** | 331.7±0.3 | 36.96 | 55±2 | 307.0±0.5 | 42.31 | 332.3±0.3 | 36.76 | 55±2 |
| **50/50** | 330.3±0.5 | 28.65 | 44±1 | 308.3±0.6 | 34.86 | 330.0±0.5 | 28.64 | 45±1 |
| **601X** | 329.7±0.3 | 23.92 | 39±2 | 309.0±0.5 | 31.45 | 330.0±0.5 | 23.71 | 39±2 |

The crystallinity of the sintered billets decreases with increasing molecular weight. This is expected as the lower molecular weight chains have more mobility to crystallize. The

second heating scans also show the same trend, indicative of melt memory formed during the sintering process as the DSC results of un-sintered billets do not show this result.

WAXS of sintered billets are shown in Figure 20 and Table V.

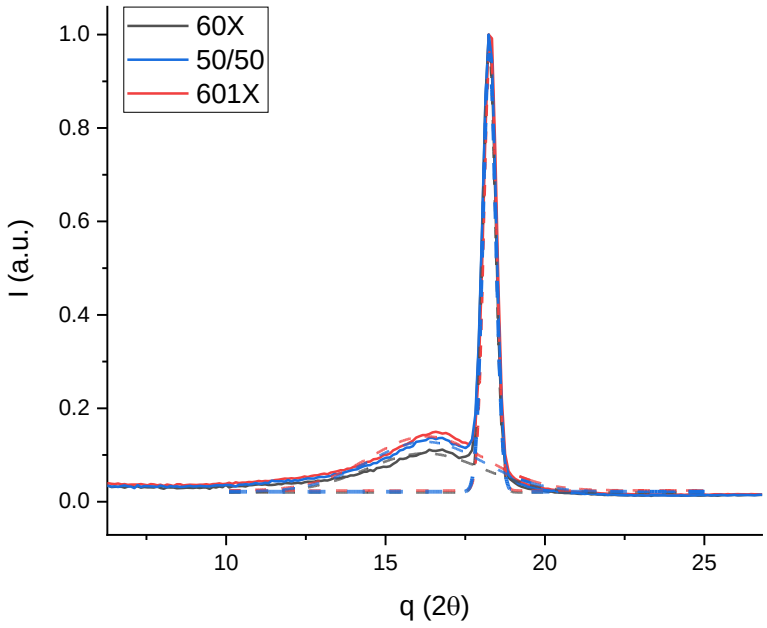


**Figure 20:** WAXS of sintered billets.

**Table V:** WAXS analysis of sintered billets.

| **Specimen** | **Amorphous** | | | **Crystalline** | | | | Crystallinity (wt %) |
|---|---|---|---|---|---|---|---|---|
| | 2θ (°) | Area | FWHM (°) | 2θ (°) | Area | FWHM (°) | Crystallite Size (Å) | |
| **60X** | 16.15 ±0.04 | 0.484 ±0.08 | 4.27± 0.02 | 18.16 ±0.04 | 0.580 ±0.08 | 0.477± 0.01 | 187±3 | 55±1 |
| **50/50** | 16.22 ±0.01 | 0.568 ±0.09 | 4.22± 0.01 | 18.23 ±0.01 | 0.581 ±0.09 | 0.475± 0 | 188±1 | 51±1 |
| **601X** | 16.24 ±0.01 | 0.634 ±0.10 | 4.27± 0.06 | 18.24 ±0.03 | 0.576 ±0.10 | 0.458± 0.01 | 195±3 | 47±1 |

Similar to DSC results, the crystallinity calculated using the peak areas show a decreasing trend with molecular weight. The crystallite size, calculated from the Scherrer equation, is similar for the 60X specimens and the blend, but higher for 601X.

Compressing testing results of sintered billets are shown in Figure 21 and tabulated in Table VI.

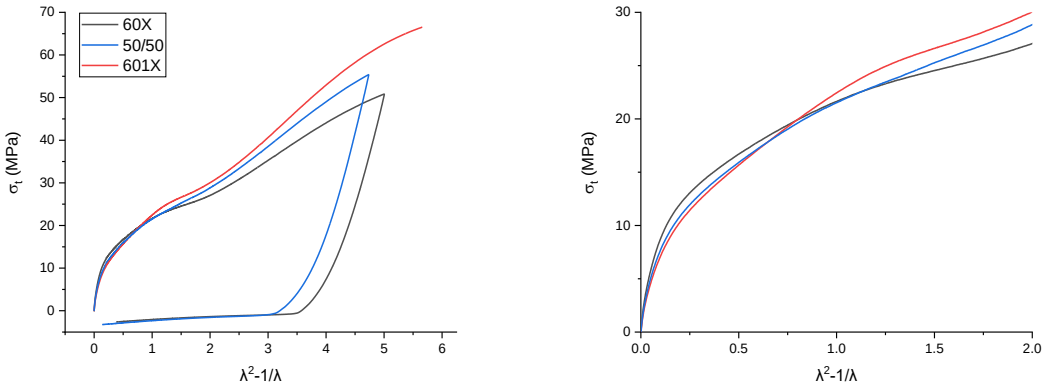


**Figure 21:** Compression testing plots of sintered billets. The loading and unloading profile is plotted on the left. The plot on the right is magnified to show the initial strain range encompassing Young's modulus and the yield stresses.

**Table VI:** Compression testing results of sintered billets. $E_0$, $G_R$, $E_u$, $\sigma_{y1}$, and $\sigma_{y2}$ are the Young's modulus, strain-hardening modulus, unloading modulus, first yield stress, and second yield stress, respectively.

| Specimen | $E_0$ (MPa) | $G_R$ (MPa) | $E_u$ (MPa) | $E_u/E_0$ | $\sigma_{y1}$ (MPa) | $\sigma_{y2}$ (MPa) |
|---|---|---|---|---|---|---|
| 60X | 101±5 | 10.4±0.6 | 16±2 | 0.16±0.03 | 12.4±0.4 | 26±1 |
| 50/50 | 98±1 | 11.5±0.5 | 15±2 | 0.16±0.02 | 11.9±0.4 | 27±2 |
| 601X | 87±4 | 12.7±0.3 | 20±0 | 0.23±0.02 | 10.9±0.4 | 28±1 |

Two yield points, $\sigma_{y1}$ and $\sigma_{y2}$ are observed at Green strains of 0.25 and 1.25, respectively. A similar phenomenon is observed in polyethylene. Due to a fine and coarse slip deformation mechanism, the first yield point occurs due to initial disruption of lamellae

(fine slip) described by mild lattice displacement. At the second yield point, significant disruption takes place as lamellae displacement occurs over multiple crystallographic planes (coarse slip).[22] Young's modulus decreases with molecular weight while strain hardening modulus increases. It was already shown that the final density of these samples is similar and thus are probably not responsible for these trends. Instead, the decrease in Young's modulus is a result of decreasing crystallinity. The increasing strain hardening modulus, however, is a result of increased entanglements or tie molecule density due to the increased molecular weight. Finally, unloading moduli are significantly less than Young's moduli, indicating that most of the energy stored in the system from the first loading is irreversible.

## 2.4 Conclusions

Varying the PTFE grade showed significant effects in both sintering behavior and final billet properties. During sintering, the maximum normalized height ratio and anisotropy factor increased with molecular weight, indicating that more latent free energy is stored during compaction as molecular weight increases. Both Young's modulus and crystallinity of the sintered billets decreased with molecular weight. Interestingly, the sintering kinetics of the blend was slower than the pure specimens. This shows that it is not advantageous to blend PTFE powders for commercial sintering processes as blends are delayed in sintering during both recovery and densification. Some of these same techniques can be used to also study newer sintering processes, such as Selective Laser Sintering (SLS) 3D printing, an additive manufacturing process. This will be discussed in Chapter 5 of this dissertation.

# CHAPTER 3

# UPCYCLING BY GRAFTING ONTO SEMI-CRYSTALLINE POLYMERS USING SUPERCRITICAL $CO_2$

## 3.1 Introduction

The on-going demand for mitigating environmental consequences of plastic waste is an apparent and challenging global endeavor. Currently, less than 10% of plastic waste in the United States is recycled each year. This is due, in part, to economic constraints inherent to current recycling strategies.[23–25] For example, grinding and remelting of plastic causes degradation, reducing the quality and therefore value of the material compared to the virgin resin. Additionally, sorting of plastic waste is a tedious, time-consuming prerequisite that is required due to the incompatibility of waste streams.[25,26] Hence, there is need to develop new strategies for polymer upcycling to compatibilize immiscible waste streams as well as add value to widely used plastics.[27] It is therefore necessary to economically generate compatibilizers from commodity and engineering plastics for next generation polymer blends, alloys, and composites.

The stability of immiscible blends is traditionally improved by incorporating a compatibilizer in the form of a copolymer.[28,29] The simplistic case is a linear A-B block copolymer which is added to an immiscible blend of polymers A and B. Because each block is miscible with one of the two blended components, the block copolymer lowers the interfacial energy by migrating to interfaces, allowing for smaller domain sizes.[28] Recent studies have shown this compatibilization effect with various blends. For example, the

morphology of polylactide (PLA) and poly(ε-caprolactone) (PCL) was controlled using poly(methoxy poly(ethylene glycol) monomethacrylate-co-1-vinyl- 3-ethylimidazolium bromide) (P[MPEGMA-IL]).[30] Additionally, poly(butylene terephthalate) was toughened by blending with thermoplastic polyurethane (TPU) using the terpolymer, poly(ethylene-butylacrylate-glycidyl methacrylate) (PTW) as a compatibilizer.[31]

Block copolymers have demonstrated a breadth of other applications that involve combining beneficial properties of two or more blocks. Thermoplastic elastomers, for example, are copolymers of glassy and rubbery blocks, exhibiting rubber elasticity combined with the processing feasibility of a thermoplastic. It has also been demonstrated that drug encapsulation and delivery is facilitated by amphiphilic block copolymers which form a micellular structure. Drugs which are encapsulated within these micelles can be transported at concentrations above their water solubility.[32] Additionally, directed self-assembly of block copolymers in sub-micron domains allow for patterning applications in soft lithography.[33] Block copolymers have also been extensively used as impact modifiers as they phase separate into rubbery domains when blended with thermoplastics.[34] These domains then cavitate and allow for energy dissipation to take place during a fracture process.

Graft copolymers are a specific type of copolymer where side chains are attached to a linear backbone. This architecture is advantageous in that a specific design can be tailored to allow for a wider range of morphological control compared to traditional block copolymers. One can tune the backbone molecular weight, grafting density, grafting molecular weight, number of end-groups, etc. to achieve desired physical properties.[35] For

example, bottlebrush polymers are graft copolymers whose side chains are polymeric. When densely grafted, bottlebrush polymers afford a branched structure which does not entangle.[36] This allows for lower process viscosity when incorporated in blends as compatibilizers or impact modifiers. The tradeoff, however, is controlling the architecture involves complicated synthetic procedures that normally require multiple steps. In situations where one desires to establish block structures that selectively contain grafts, each block must be synthesized independently or protected preceding a subsequent grafting step.[36]

A possible approach to achieving morphological selectivity while reducing synthetic complexity is to polymerize selectively into the amorphous regions of a semi-crystalline polymeric backbone while leaving the crystalline domains unmodified. Conditions are thus required to be at temperatures below melting in solvents that do not dissolve the backbone. Given its mild critical point (31°C, 7.4 MPa),[37] supercritical $CO_2$ has been used to create immiscible blends by polymerizing a monomer, below melting, within the amorphous regions of semi-crystalline polymeric matrices.[38] It is known that supercritical $CO_2$ is confined to the amorphous regions due to size exclusion from the denser, crystalline phase.[39,40] Rapid monomer transport is also facilitated as supercritical $CO_2$ exhibits the density of a liquid and the diffusivity of a gas.[41] Therefore, one can imagine exploiting these transport properties to create unique materials, including multi-phase materials,[42–45] as well as composites containing additives.[46–50] Additionally, in contrast to many organic solvents, supercritical $CO_2$ is inexpensive, non-toxic, non-flammable, and environmentally benign when fully recovered during processing.

Therefore, using this as a processing medium to perform selective graft chemistry on semi-crystalline plastics provides a cost-effective, sustainable method for polymer upcycling. Accordingly, A-B, A-B-A, A-B-A-B-A… etc. block structures are generated where block "B" exhibits a bottlebrush architecture. A schematic of this morphology is shown in Figure 22.

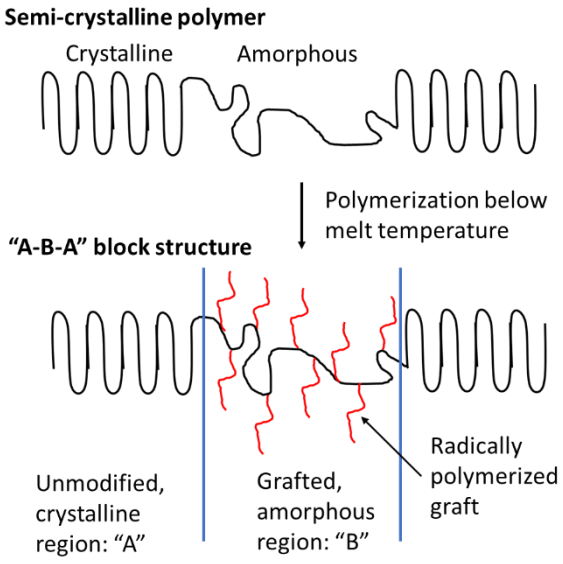


**Figure 22:** Selective morphology of semi-crystalline grafted copolymer.

Nayak,[51] Mukherjee,[52] and El-Rafie[53] have performed various investigations on graft polymerization of vinyl monomers onto nylon fibers. Of the methods used, radical initiation is the most relevant to the scope of this work. In these cases, fibers were immersed in solutions of monomer and free radical initiator. Polymerization then proceeded without disrupting the integrity or crystallinity of the polyamide. The grafting reaction was stipulated to occur by the formation of macroradicals via hydrogen atom abstractions of the polyamide backbone. The same grafting strategy was later implemented on thin

polyamide films[54] and membranes.[55] While appreciable incorporation of the free radically polymerized material was observed via mass increase in both fibers and films, detailed investigations to differentiate whether the polymer was covalently bound to the polyamide versus kinetically trapped were not performed beyond the surface level. Additionally, grafting in bulkier polyamide geometries was not explored as maximum specimen thicknesses were on the order of 100 μm. More recent work by Coltelli[56] has demonstrated bulk free radical grafting of polyamide 6 through short and long chain branching using diethyl maleate (DEM) and dicumyl peroxide (DCP). However, morphological selectivity was not possible as these grafting reactions were performed in the melt.

Although blends have been made in supercritical $CO_2$, fabricating semi-crystalline graft copolymers using this medium has been insufficiently investigated. Few attempts have been made using this approach on polyolefins, for example, grafting onto polypropylene,[57] and polyethylene.[58] However, the graft yield, the portion of polymer which covalently bonds to the polyolefin relative to the total polymerized within the amorphous regions, was minimal in these cases, not exceeding 10 wt %. Further studies are warranted, to assess the effectiveness of this technique on a broader range of semi-crystalline polymers. The role of the semi-crystalline polymer on grafting efficacy would thus be elucidated.

In this work, grafting is achieved by immersing a semi-crystalline polymer in a solution of a vinyl monomer, free radical initiator, and an optional cosolvent. Free radical polymerization of the monomer is then performed in the presence of supercritical $CO_2$. Conditions are set above the critical point of $CO_2$, but below the melt temperature of the

semi-crystalline polymer such that the crystalline phase is preserved. Grafting is performed on three semi-crystalline polymers: polyamide 6 (PA6), polyethylene terephthalate (PET), and isotactic polypropylene (iPP). Characterization of each polymer as well as the grafting yield is presented. The influence of the semi-crystalline polymer on the graft yield is discussed herein. Following this study, PA6 graft copolymers are further characterized to assess thermal properties, moisture resistance, and grafting molecular weight. Additionally, di(ethylene glycol) methyl ether methacrylate is polymerized within PA6 using the same grafting procedure and swelling experiments are performed to assess whether hydrophilicity can be achieved in contrast to the hydrophobic grafted polystyrene (PS). Thus, potential added value to this widely used engineering plastic from the grafting process is assessed and discussed herein.

## 3.2 Materials and Methods

1 mm thick PA6 and 0.5 mm thick PET sheets were purchased from Goodfellow. Sheets were cut into films of length x width no greater than 80 mm x 16 mm before use. iPP pellets were provided by ExxonMobil and compression molded to 1 mm thick plaques at 200°C for 15 minutes. A film was then cut to dimensions of 50 mm x 9 mm length x width before use. PA6 powder was provided by BASF and used as received. Styrene, tert-butyl peroxybenzoate (TBPB), methanol, m-cresol, p-xylene, cyclohexane, and acetone were purchased from Millipore Sigma. Styrene was filtered through an aluminum oxide column before use to remove inhibitors. All other chemicals were used as received, without further purification.

### 3.2.1 Processing in $scCO_2$

Polymerizations were performed in pressurized batch reactors purchased from High Pressure Equipment Company. During each process, semi-crystalline polymeric material was immersed in a solution composed of styrene monomer and TBPB free-radical initiator. An initiator concentration of 0.3 mol % relative to the monomer was used. For PA6 specimens, a methanol co-solvent of 50 vol % relative to the monomer was used. Following the insertion of the specimen and solution, the reactor was then sealed, and heating and $CO_2$ pressurization was applied until the desired supercritical conditions were achieved. For each polymerization, pressure was held constant at 28 MPa for 39 hours while temperature was held at 75°C for 24 hours, then 115°C for 15 hours. After processing, the reactor was cooled to room temperature, then gradually depressurized to atmospheric conditions. A schematic of the reactor setup is shown in Figure 23.

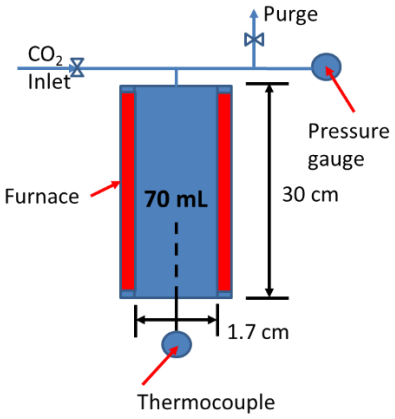


**Figure 23:** Schematic of reactor setup.

Specimens were then removed, washed with toluene to remove any excess homopolymer on surfaces, and vacuum dried at 80°C for at least 12 hours. Samples were

weighed before and after processing to determine the mass fraction of incorporated PS. PS composition was determined via equation (3.1)

$$P_m = \frac{w_m - w_u}{w_m} \tag{3.1}$$

where $P_m$ is the PS composition of the modified specimen, $w_m$ is the weight of the dried, modified specimen, and $w_u$ is the weight of the unmodified specimen.

### 3.2.2 Specimen Purification

In general, the modified specimens will include some fraction of un-grafted semi-crystalline polymer, grafted semi-crystalline polymer as well as un-grafted homopolymer PS, and grafted PS. Determination of grafting therefore requires the removal of homopolymer PS from the modified specimens. This was accomplished using a three-step procedure. First, a maximum of 0.1 g of each modified specimen was dissolved in 1-2 g of cosolvent. Next, antisolvent which dissolves PS but not the semi-crystalline polymer was added to each solution in excess (13-15 g). Homopolymer PS thus remained dissolved such that the precipitate formed was free of PS homopolymer. Finally, the precipitates were collected and repeatedly washed with the antisolvent to complete the purification process. They were then dried in a vacuum oven at 80°C for at least 12 hours. Solubility parameters of each component and solvents chosen for each specimen are shown in Table VII and Table VIII.

**Table VII:** Hildebrand solubility parameters of relevant polymers and solvents.[59]

| Component | $\delta_h$ ($MPa^{0.5}$) |
|---|---|
| PS | 18.3 |
| PA6 | 25.5 |
| PET | 22 |
| iPP | 16.6 |
| m-cresol | 27.2 |
| xylene | 18.2 |
| cyclohexane | 16.8 |

**Table VIII:** Cosolvents and antisolvents used for extraction of PS homopolymer in each specimen.

| Specimens | Cosolvent | Antisolvent |
|---|---|---|
| PA6 | m-cresol | cyclohexane |
| PET | m-cresol | cyclohexane |
| iPP | p-xylene | cyclohexane |

Fourier Transform Infrared (FTIR) spectra were recorded with a Perkin-Elmer Spectrum One Fourier transform infrared spectrometer directly on unmodified specimens and purified precipitates.

### 3.2.3 Thermal Analysis

Differential scanning calorimetry (DSC) was performed using a TA Instruments Q200 Differential Scanning Calorimeter equipped with RCS90 device for low temperatures. On all specimens, two heating scans were performed with one cooling cycle in between. The temperature range was 0 to 250°C for all specimens except for PET, where the temperature range was 0 to 300°C. Heating and cooling rates were 10 K/min. For each specimen, the areas of melt endotherms were used to determine their crystallinity.

If the crystalline phase were preserved during polymerization, the measured crystallinity of modified specimens would be less than the unmodified specimens commensurate with the weight fraction of incorporated amorphous PS. To verify this, PS composition, $P_m$, was calculated using equation (3.2)

$$P_m = 1 - \frac{Xc_m}{Xc_u} \tag{3.2}$$

where $Xc_m$ and $Xc_u$ are the crystalline weight fractions measured from the first heating scans of the modified and unmodified specimens, respectively. Results were compared to the measured weight fractions determined by equation (3.1).

Analogously, PS compositions of purified specimens were determined using equation (3.3)

$$P_p = 1 - \frac{Xc_p}{Xc_u} \tag{3.3}$$

where $P_p$ is the PS composition of the purified specimen (i.e. the grafted PS), $Xc_p$ is the crystallinity of the purified specimen, and $Xc_u$ is the crystallinity of the unmodified specimen. In contrast to equation (3.2), crystallinity measurements from second heating scans were used to eliminate the recrystallization history from precipitation during the extraction process.

### 3.2.4 Solid-State NMR

$^{13}C$ Solid-State NMR was performed on purified specimens as another method to determine the composition of grafted PS. For the iPP specimen, direct polarization was used to ensure quantitative validity. For PET and PA6 specimens, cross polarization was used given their similarities in segmental mobility to PS. Since non-protonated carbons are

underrepresented in cross polarization, integrations of peaks corresponding to only CH and $CH_2$ carbons were used in compositional calculations. In all cases, 8 kHz MAS was applied at an angle of 45° with a delay time of 30 s.

The graft yield was calculated using equation (3.4)

$$G = \frac{P_p}{P_m} \tag{3.4}$$

Yield results using PS compositions from both DSC and ssNMR were compared for each specimen.

### 3.2.5 Moisture Uptake Experiments

Following this analysis, further investigations were performed on additional PA6 specimens to gain a property analysis with varying PS compositions. DSC was performed using the same procedure as discussed previously to compare glass transition temperatures as well as the remelting behavior. Moisture uptake experiments were performed on processed films of varying compositions where weight change was measured over a two-week period at 70°C and 76% relative humidity. The data were fit to Fick's second law[60] as represented by equation (3.5)

$$M(t) = M_\infty \left[1 - exp\left(-7.3\left(\frac{D*t}{h^2}\right)^{0.75}\right)\right] \tag{3.5}$$

where M is the moisture uptake, $M_\infty$ is the equilibrium moisture uptake, D is the diffusivity constant, t is time, and h is specimen thickness. The diffusivity constant was calculated using equation (3.6)

$$D = \pi\left(\frac{h}{4M_\infty}\right)^2 (m)^2 \tag{3.6}$$

where m is the slope of the initial linear region of the moisture uptake curve.

### 3.2.6 Measurement of Grafting Molecular Weight

In yet another analysis, the effect of polymerization temperature on grafting molecular weight was studied. Polymerization temperatures of 115°C and 130°C were used. Grafting molecular weights were measured by exposing the processed specimens to superheated water, hydrolyzing the PA6 such that the remaining PS can be characterized. This was done in a batch reactor where specimens were submerged in water, then pressurized at 14 MPa at a temperature of 250°C for 12 hours. Following this, specimens were purified by dissolution in chloroform, then precipitated using methanol. PS molecular weight was then determined via end-group analysis from $^{1}$H NMR in chloroform-$d_1$ and Gel Permeation Chromatography (GPC) in THF relative to PS standards. These results were compared to theoretical values calculated using the following procedure:[61]

The number average molecular weight, $\bar{M}_n$, assuming that termination predominantly occurs by radical coupling, is given by equation (3.7)

$$\bar{M}_n = M_o \bar{X}_n \tag{3.7}$$

where $M_o$ is the molecular weight of the monomer repeat unit and $\bar{X}_n$ is the number of repeat units, given by equation (3.8):

$$\bar{X}_n = 2\nu \tag{3.8}$$

where ν is the kinetic chain length. ν can be calculated using equation (3.9):

$$\nu = \frac{k_p[M]}{2(f k_d k_t [I])^{1/2}} \tag{3.9}$$

where f, [M], and [I] are the initiator efficiency, monomer concentration, and initiator concentration, respectively. $k_p$, $k_d$, and $k_t$, are rate constants for free radical propagation, disproportionation, and termination, respectively. These can be calculated using the Arrhenius equation (3.10):

$$k_i = A_i e^{-E_i/RT} \tag{3.10}$$

where $A_i$ is a constant, $E_i$ is activation energy, and T is temperature. $k_d$ can be calculated using equation (3.11):

$$k_d = \frac{0.693}{t_{1/2}} \tag{3.11}$$

where $t_{1/2}$ is the initiator half-life. Values used in these equations for free-radical polymerization of styrene with tert-Butyl peroxybenzoate are shown Table IX and Table X.

**Table IX:** Temperature-independent values, monomer concentration, and initiator concentration.

| $M_o$ (g/mol) | $A_p$ (L/mol/s) | $E_p$ (J) | $A_t$ (L/mol/s) | $E_t$ (J) | [M] (mol/L) | [I] (mol/L) |
|---|---|---|---|---|---|---|
| 104 | 4.5E6 | 26000 | 5.8E8 | 8000 | 4.35 | 1.31E-2 |

**Table X:** Temperature-dependent values and molecular weight calculations. An initiator efficiency of 1 was used.

| Temperature (°C) | $t_{1/2}$ (s) | $k_d$ ($s^{-1}$) | $k_p$ (L/mol/s) | $k_t$ (L/mol/s) | ν | $\bar{X}_n$ | $\bar{M}_n$ (kDa) |
|---|---|---|---|---|---|---|---|
| 115 | 6575 | 1.05E-4 | 1422 | 4.86E7 | 378 | 756 | 79 |
| 130 | 1174 | 5.90E-4 | 1919 | 5.33E7 | 206 | 412 | 43 |

### 3.2.7 Grafting with Diethylene Glycol Methyl Ether Methacrylate

Finally, dietheylene glycol methyl ether methacrylate ($MEO_2MA$) was used as another monomer and subjected to the same processing within a PA6 film. Water uptake was performed and compared to a control PA6 sample.

## 3.3 Results and Discussion

### 3.3.1 Processing in $scCO_2$

It was apparent that all specimens swelled after the grafting procedure due to the incorporation of PS within each matrix. This can be seen in Figure 24, which shows the iPP specimen before and after processing.


**Figure 24:** Picture of unmodified (u) and modified (m) iPP plaque.

The PS composition of each specimen determined by equation (3.1) is shown in Table XII. Compositions determined by equation (3.2) were gathered from crystallinity measurements using DSC. Traces for the PA6 specimen are shown in Figure 25.

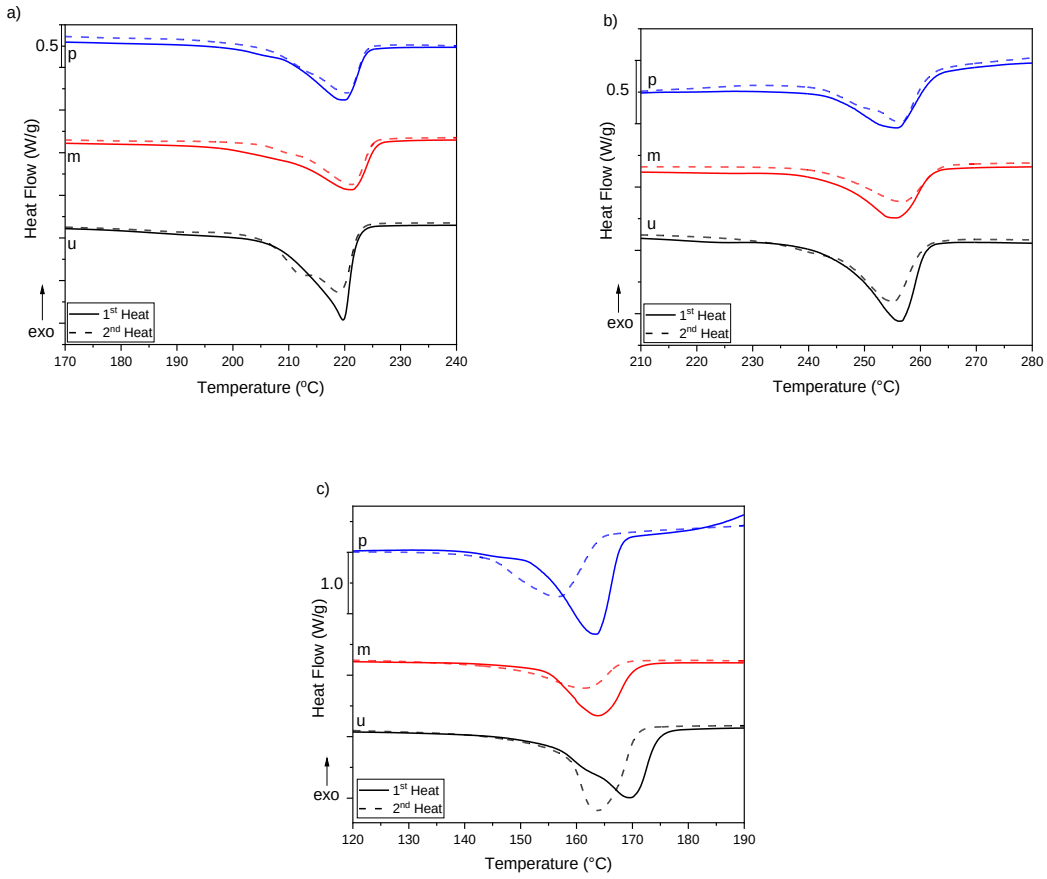


**Figure 25:** DSC plots of the unmodified (u), modified (m), and purified (p) PA6 (a), PET (b), and iPP (c) specimens.

Melting enthalpies were measured to determine the crystallinity resulting from both heating scans. This was analogously performed with the PET and iPP specimen. Values from each thermogram are tabulated in Table XI. It should be noted that 2-3 runs were performed on purified specimens to assess repeatability as the graft yield results rely heavily on their crystallinity measurements. As can be seen, the margins of error are miniscule.

**Table XI:** Crystallinity measurements from first and second heating scans for unmodified (u), modified (m), and purified (p) specimens. Heats of fusion used to calculate crystallinity were 230, 140, and 207 J $g^{-1}$ for PA6, PET, and iPP, respectively.[21]

| Specimen | | 1st Heat | | | 2nd Heat | | |
|---|---|---|---|---|---|---|---|
| | | $T_m$ (°C) | $\Delta H_m$ (J $g^{-1}$) | $X_c$ (wt %) | $T_m$ (°C) | $\Delta H_m$ (J $g^{-1}$) | $X_c$ (wt %) |
| **PA6** | u | 220 | 64 | 28 | 219 | 64 | 28 |
| | m | 221 | 41 | 18 | 221 | 37 | 16 |
| | p | 220 | 44±0 | 19±0 | 220 | 41±1 | 18±0 |
| **PET** | u | 256 | 52 | 37 | 255 | 49 | 35 |
| | m | 256 | 34 | 24 | 257 | 24 | 17 |
| | p | 256 | 43±2 | 31±1 | 256 | 39±1 | 28±1 |
| **iPP** | u | 170 | 104 | 50 | 164 | 110 | 53 |
| | m | 164 | 57 | 28 | 161 | 50 | 24 |
| | p | 164 | 113±0 | 55±0 | 163 | 104±2 | 50±1 |

As can be seen from the table, no significant changes in $T_m$ are observed when comparing the unmodified (u), modified (m), and purified (p) specimens while $X_c$ varied significantly. This is expected as supercritical $CO_2$ does not penetrate the crystalline regions when processed below melting while $X_c$ will vary commensurate with the incorporated fraction of amorphous PS. Composition calculations based on $X_c$ were performed using equation (3.2). Results are shown in Table XII and compared with the results from equation (3.1).

**Table XII:** Weight measurements of unmodified ($w_u$) and modified ($w_m$) specimens. $P_m$, the composition of PS in the modified specimens, calculated by equations (3.1) and (3.2), are shown.

| Specimen | $w_u$ (g) | $w_m$ (g) | (1) $P_m$ (wt %) | (2) $P_m$ (wt %) |
|---|---|---|---|---|
| PA6 | 2.15 | 3.27 | 34 | 36 |
| PET | 0.45 | 0.68 | 34 | 35 |
| iPP | 0.46 | 0.96 | 52 | 44 |

As can be seen, equations (3.1) and (3.2) are in strong agreement for PA6 and PET indicating preservation of the crystalline phase. The slight offset in iPP where $P_m$ from equation (3.2) is less than that of equation (3.1) indicates the crystallinity of the iPP specimen increased slightly during processing. It has been shown that annealing of iPP below melting can impart morphological changes such as an increase in crystallinity.[38] Thus, this observed result is within reason and is unlikely related to the grafting chemistry.

### 3.3.2 Specimen Purification

Purification of the material was performed because the modified specimens can contain both ungrafted and grafted PS. Determining whether PS was grafted and, if so, the amount of grafting that occurred, required removal of the homopolymer PS. To achieve this, purification was implemented using various solvents from the extraction process described previously. In all cases, sufficient precipitates were collected for further characterization.

FTIR was performed on purified specimens and compared to unmodified homopolymers to detect for PS. Spectra are shown in Figure 26.

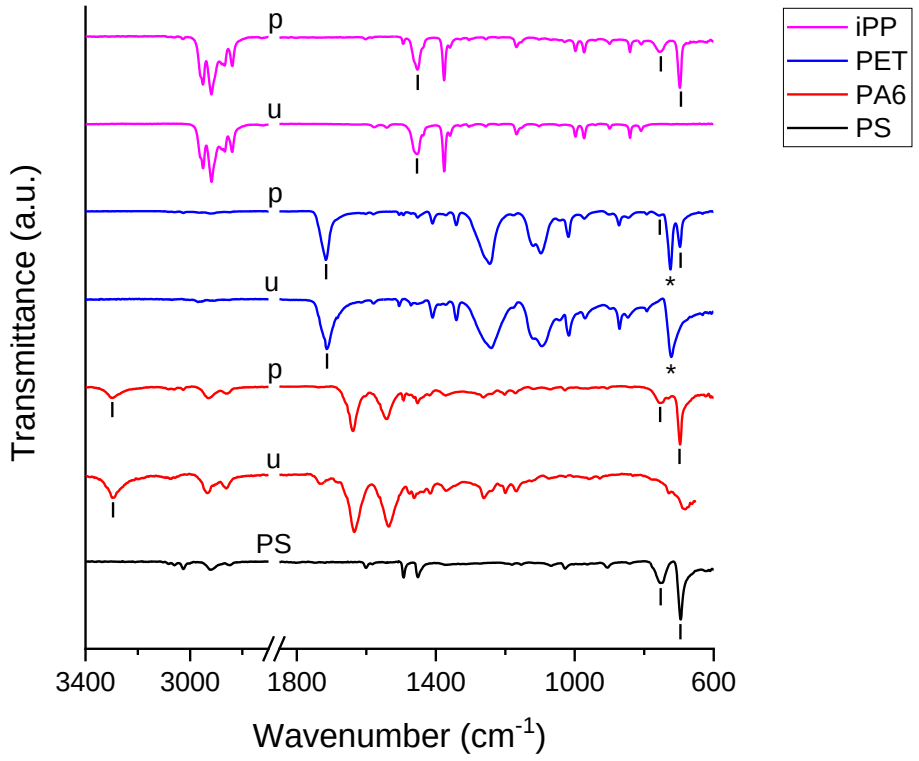


**Figure 26:** FTIR of unmodified (u) and purified (p) PA6, PET, and iPP specimens. Spectra of the PS homopolymer is also shown for comparison.

Peaks at 695 $cm^{-1}$ and 755 $cm^{-1}$ are indicative of monosubstituted benzene from PS and the peak at 3,300 $cm^{-1}$ represents the PA6 secondary amine. Additionally, the peak at 1700 $cm^{-1}$ represents the ester carbonyl in PET and the peak at 1400 $cm^{-1}$ corresponds to the iPP methyl group. It should be noted that the PET specimens show a peak at 725 $cm^{-1}$, labeled as (*), corresponding to the di-substituted phenyl moiety. In the purified PET specimen, this peak overlaps with the PS monosubstituted doublet, causing its signature to dampen. In this case, the peak at 755 $cm^{-1}$ is barely visible. Regardless, peaks indicative of both the

semi-crystalline polymer and PS were apparent in all purified specimens, revealing that grafting has occurred as the homopolymer PS was removed during the purification process.

### 3.3.3 Determination of Graft Yield using DSC

While this result is sufficient to elucidate grafting, it does not provide details on the grafting efficacy, that is, the quantity of covalently bound PS versus homopolymer PS produced in these specimens. Additional characterization is thus required for such quantification. One potential metric is to use the crystallinity measurements of purified specimens and calculate PS composition as was done with modified specimens using equation (3.3). Graft yield can then be determined by comparing this to the PS composition of the respective modified specimens. Since the purified material was recrystallized from solution, comparisons were drawn using crystallinity measurements from second heating scans to eliminate the thermal history. PS compositions of modified and purified specimens were calculated from equation (3.2) and (3.3), respectively, using crystallinity measurements from second heating scans. Graft yield was then calculated using equation (3.4). Results are shown in Table XIII.

**Table XIII:** Graft yield results (G) using PS compositions of modified ($P_m$) and purified ($P_p$) specimens calculated by crystallinity from second heating scans.

| Specimen | $P_m$ (wt %) | $P_p$ (wt %) | G (%) |
|---|---|---|---|
| PA6 | 43 | 36 | 84 |
| PET | 51 | 20 | 39 |
| iPP | 55 | 6 | 11 |

It should be noted that the PS compositions used for determining graft yield are indirect because calculations were drawn from crystallinity values measured during second

heating scans, where recrystallization occurred during a preceding cooling step. For crystallinity measurements to be accurately indicative of PS composition, the crystallinity must be unaffected by the PS grafts or presence of PS homopolymer. Although this assumption was implicit in equations (3.2) and (3.3), it should not be ignored that PS may affect the crystallization behavior. For example, PS grafts may introduce confinement which can disrupt the crystallization of neighboring backbone regions. Additionally, PS present in the system may act as nucleation sites. Any influence of crystallization behavior such as the phenomena described can affect the crystallinity as measured during second heating scans. This would in turn compromise the validity of using this approach to calculate PS composition and subsequent graft yield results.

### 3.3.4 Determination of Graft Yield using ssNMR

Due to the previous concerns, solid-state NMR was used as another technique to quantify the PS compositions of purified specimens and thus, graft yield. Comparisons were then drawn with values calculated from DSC measurements to assess the reliability of each approach. ssNMR was performed on the purified specimens. The spectra are shown in Figure 27.

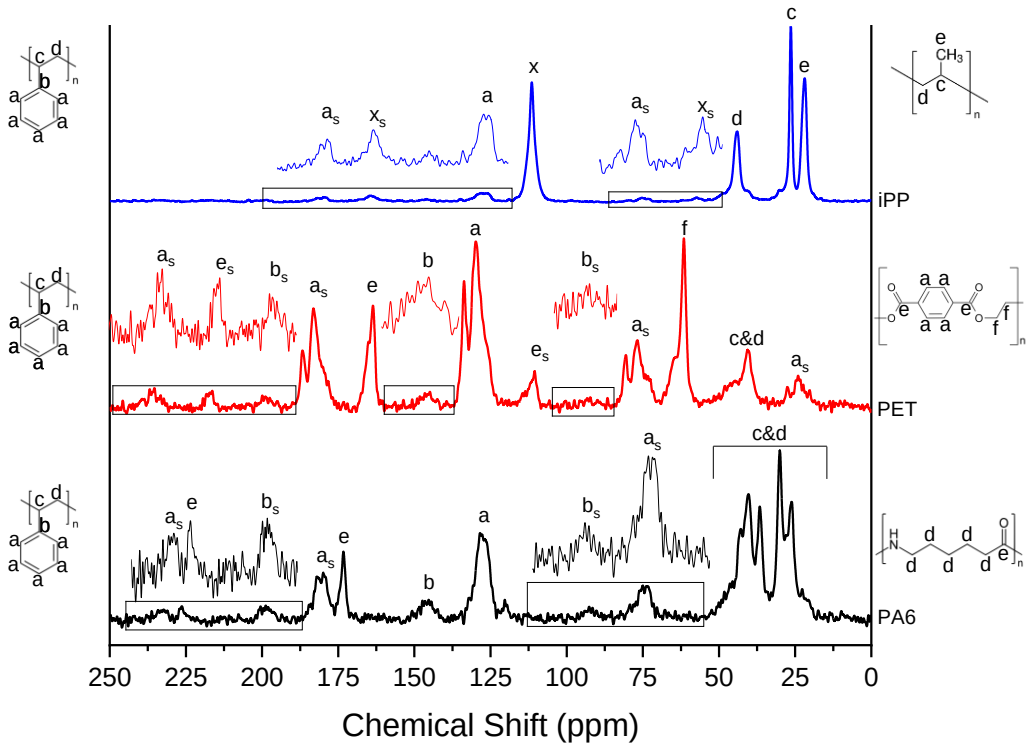


**Figure 27:** $^{13}C$ Solid State NMR of purified specimens. Peaks are labeled in accordance with the molecular structures drawn on either side of the spectra. Peaks labeled x and $x_s$ correspond to signals from the PTFE tape used to properly displace the specimen in the NMR rotor. Such signals do not interfere with the peaks needed for compositional calculations.

Chemical shifts and peak integrations of relevant signals are tabulated in Table XIV.

**Table XIV:** Chemical shifts (δ) and peak integrations (I) of relevant carbon (C) signals.

| **PA6** | | | **PET** | | | **iPP** | | |
|---|---|---|---|---|---|---|---|---|
| C | δ (ppm) | I | C | δ (ppm) | I | C | δ (ppm) | I |
| a | 128 | 5.00 | c & d | 41 | 0.70 | a | 128 | 18.7 |
| $a_s$ | 232 | 0.45 | f | 62 | 1.00 | $a_s$ | 180 | 4.81 |
| $a_s$ | 180 | 2.57 | | | | $a_s$ | 75 | 3.09 |
| $a_s$ | 75 | 2.18 | | | | e | 22 | 115 |
| c & d | 43-26 | 19.4 | | | | | | |

Using these spectra, PS composition of each specimen can be quantified with the following procedure: The total area per carbon of a repeat unit can be calculated using equation (3.12)

$$A_r = \frac{\sum_{i=1}^{n} I_i}{C_I} \tag{3.12}$$

where $A_r$ is the area per carbon of repeat unit r, $I_i$ is the integral of the ith peak corresponding to the repeat unit, and $C_I$ is the total number of carbon atoms contributing to the signal of the integrated peaks. Using this information, the mass fraction of PS in these purified specimens can be calculated in equation (3.13)

$$P_p = \frac{A_{PS} M_{PS}}{\sum A_r M_r} \tag{3.13}$$

where $P_p$ is the PS mass composition, $A_{PS}$ is the area per carbon of a PS repeat unit, $M_{PS}$ is the molecular weight of a PS repeat unit, and $M_r$ is the molecular weight of a repeat unit r.

An example of this calculation is shown below for the PA6 specimen. Using equation (3.12), both $A_{PS}$ and $A_{PA6}$ were calculated. For $A_{PS}$, the integrals of peaks corresponding to the protonated aromatic carbons, a, were used. Note that the spinning side bands, $a_s$, located in increments of 8 kHz from the parent peak were also accounted for.

$$A_{PS} = \frac{5.00 + 0.45 + 2.57 + 2.18}{5} = 2.04$$

Because the carbonyl carbon in PA6 is not protonated and thus unreliable for quantification in cross polarization mode, peaks corresponding to aliphatic carbons were used to calculate $A_{PA6}$. To accommodate for the overlap with PS aliphatic carbons, the entire region corresponding to methine and methylene carbons, c & d, was integrated as $A_{c\&d}$. In the

equation below, the area corresponding to the two PS aliphatic carbons, $2A_{PS}$, was subtracted from $A_{c\&d}$ to calculate the total integral resulting from the five PA6 methylene carbons.

$$A_{PA6} = \frac{A_{c\&d} - 2A_{PS}}{5} = \frac{19.4 - 2 * 2.04}{5} = 3.06$$

The calculation of $P_p$ was then possible and performed below.

$$P_p = \frac{2.04 * 104 \frac{g}{mol}}{2.04 * 104 \frac{g}{mol} + 3.06 * 113 \frac{g}{mol}} = 38\ wt\%$$

G was calculated by dividing this result by $P_m$ as measured from equation (3.1).

$$G = \frac{P_p}{P_m} = \frac{38}{34} = 112\ \%$$

In this case, a graft yield of 112% was calculated. Given the highest possible value of G is 100 %, this result could have been a consequence of some powder specimen loss during processing, leading to an underestimation of $P_m$.

For the remaining specimens, analogous calculations were performed. Results are tabulated in Table XV.

**Table XV:** Graft yield results calculated from ssNMR.

| **PA6** | | | | | **PET** | | | | | **iPP** | | | | |
|---|---|---|---|---|---|---|---|---|---|---|---|---|---|---|
| **$A_r$** | | **$P_p$** | **$P_m$** | **G** | **$A_r$** | | **$P_p$** | **$P_m$** | **G** | **$A_r$** | | **$P_p$** | **$P_m$** | **G** |
| **$A_{PS}$** | 2.04 | 38 | 34 | 112 | **$A_{PS}$** | 0.35 | 27 | 34 | 79 | **$A_{PS}$** | 5.31 | 10 | 52 | 19 |
| **$A_{PA6}$** | 3.07 | | | | **$A_{PET}$** | 0.50 | | | | **$A_{iPP}$** | 115 | | | |

A comparison between graft yield results from both DSC and ssNMR are plotted in Figure 28.

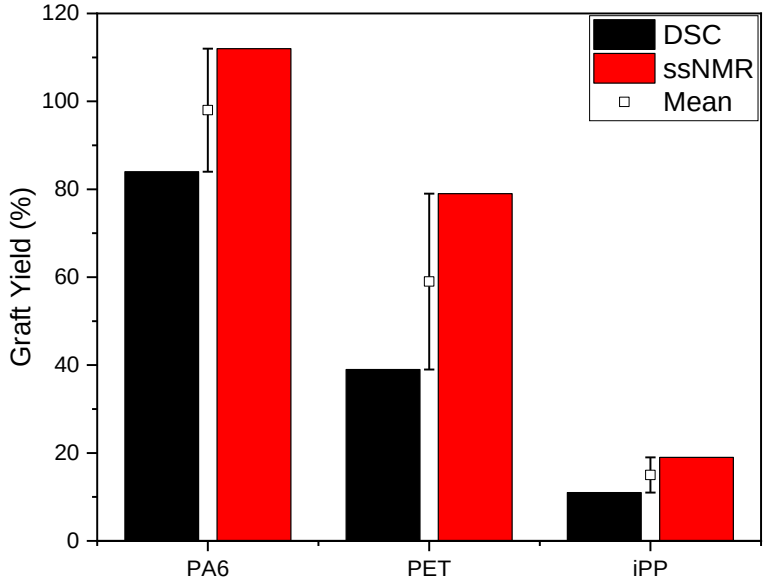


**Figure 28:** Comparison of graft yield results from DSC and ssNMR for each semi-crystalline polymer.

As can be seen, the DSC and ssNMR results differ from each other with standard deviations 14, 20, and 4 % for PA6, PET, and iPP, respectively. In all cases, DSC produced lower values of G than ssNMR. However, the validity of each technique is reinforced as both results follow the same trend, where G of PA6>PET>iPP. Additionally, the mean results are statistically different for each polymer, indicating G is dependent on the semi-crystalline polymer. Coltelli found that grafting on PA6 in the molten state was predominant on the site vicinal to the carbonyl.[56] An explanation for this is that a free radical formed on that site via hydrogen abstraction is stabilized by resonance. Using this logic, one can compare the stability of grafting sites to the other polymers in this study. For

example, the most stabilized site for a radical to form on PET would be vicinal to the oxygen due to the electron donating effect. For iPP, no such stabilization exists. Therefore, the stability of radicals formed on PA6>PET>iPP. This is consistent with the measured graft yield results.

### 3.3.5 Thermal Properties of PS-PA6 Graft Copolymers

Due to the remarkable yield in PA6, further investigation was performed on additional specimens to determine whether useful properties were gained by creating graft copolymers from this material. DSC thermograms for grafted specimens of contrasting PS compositions are shown in Figure 29. Readings are tabulated in Table XVI.

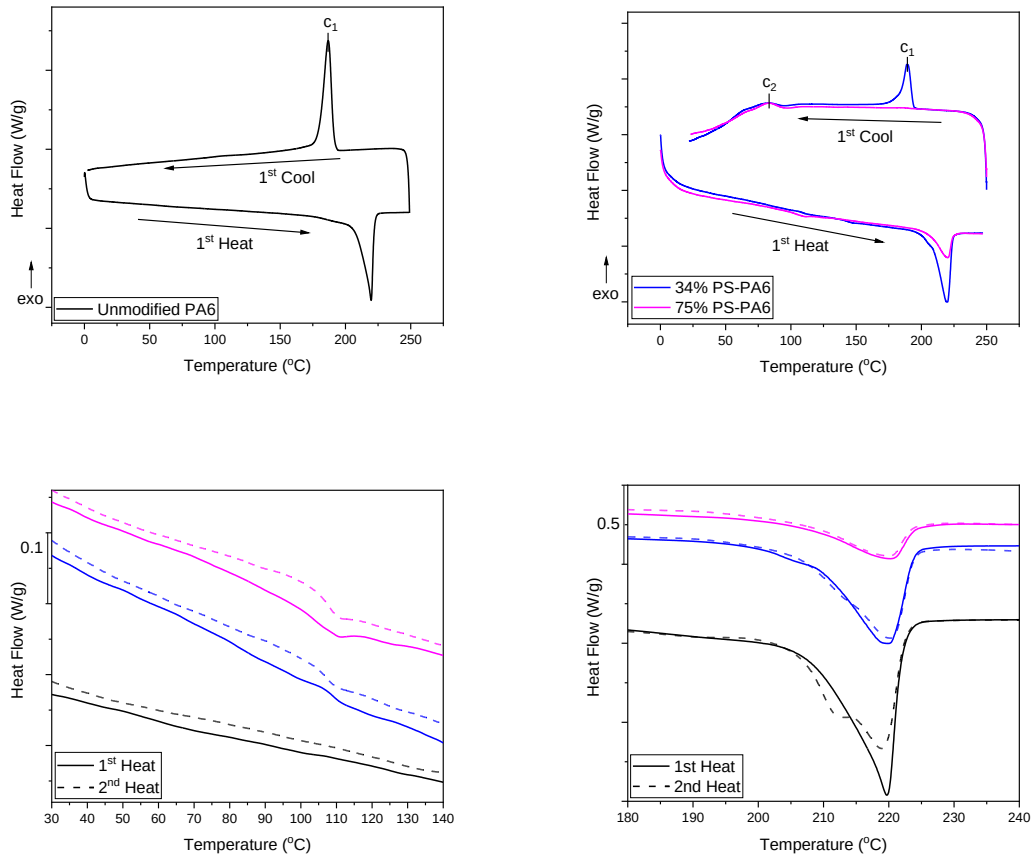


**Figure 29:** DSC of purified PA6 specimens containing 34 wt % PS (blue) and 75 wt % PS (magenta). Unmodified PA6 (black) is included for comparison.

**Table XVI:** Values of crystallization temperature, melt temperature, and crystallinity measured from each heating/cooling cycle. Unmodified PA6 is denoted as 0 wt % PS.

| PS (wt %) | 1st Heat | | | | 1st Cool | | | | 2nd Heat | | | |
|---|---|---|---|---|---|---|---|---|---|---|---|---|
| | $T_g$ (°C) | $T_m$ (°C) | $\Delta H_m$ (J $g^{-1}$) | $X_c$ (wt %) | $T_{c1}$ (°C) | $\Delta H_{c1}$ (J $g^{-1}$) | $T_{c2}$ (°C) | $\Delta H_{c2}$ (J $g^{-1}$) | $T_g$ (°C) | $T_m$ (°C) | $\Delta H_m$ (J $g^{-1}$) | $X_c$ (wt %) |
| 0 | 61 | 220 | 64 | 28 | 187 | 64 | - | - | 45 | 219 | 64 | 28 |
| 34 | 104 | 220 | 44 | 19 | 189 | 20 | 83 | 21 | 108 | 220 | 41 | 18 |
| 75 | 109 | 220 | 19 | 7 | - | - | 83 | 17 | 107 | 220 | 18 | 8 |

The grafted specimen containing 34% PS exhibits two crystallization exotherms: 189°C and 83°C. The exotherm at 189°C is similar to unmodified PA6 and expected. The additional low temperature exotherm, however, is unique to both grafted specimens. Further, the specimen containing 75% PS only displays an exotherm at the lower temperature, indicating the PS grafts inhibited crystallization. Additionally, the melt endotherms from first and second heating scans exhibit the same degree of crystallinity, demonstrating potential to melt blend these graft copolymers as compatibilizers in waste streams. Singular, glass transition temperatures above 100°C were observed for both specimens, showing no PS composition dependance. This high $T_g$ is beneficial for enhanced stiffness, as well as chemical and moisture resistance. It should be noted that the PA6 $T_g$ at 61°C appears as a very weak transition using this technique. Therefore, the grafted specimens may have an additional glass transition temperature which resembles PA6, though not apparent in these data.

### 3.3.6 Moisture Uptake Experiments

Moisture uptake experiments were also performed on 1mm thick film specimens of varying PS compositions. Results are shown in Figure 30.

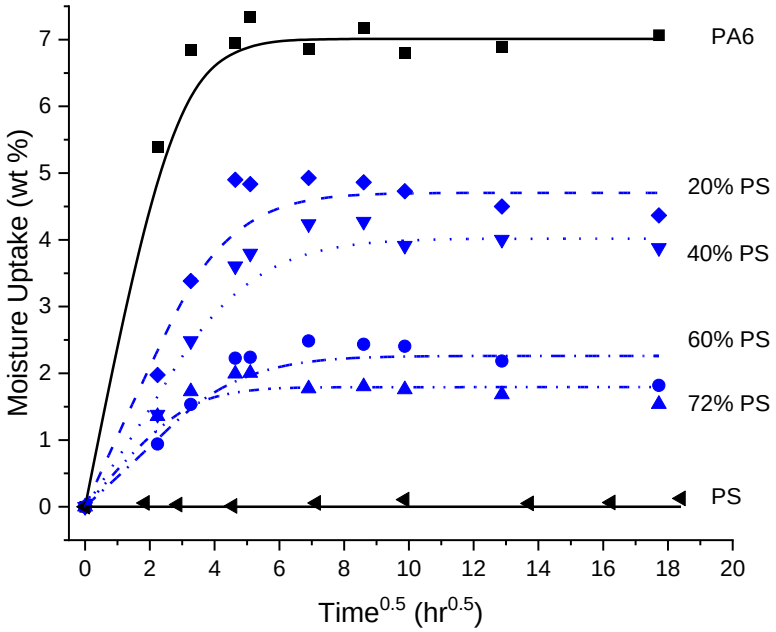


**Figure 30:** Moisture uptake of PA6 specimens exposed at 70°C and 76% relative humidity. Data were fit to Fick's second law.[60]

Details of the fit are shown in Figure 31.

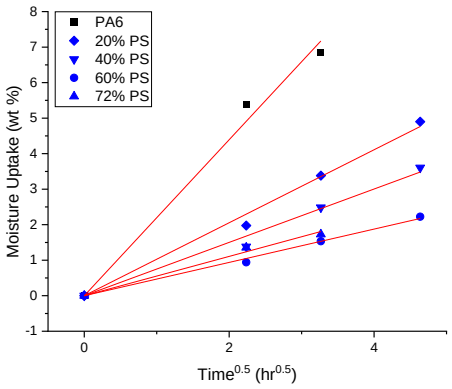


| Specimen | PA6 |
|---|---|
| Equation | y = a + b*x |
| Intercept | 0 |
| Slope | 2.19632 ± 0.1043 |
| Residual Sum of Squares | 0.34142 |
| Pearson's r | 0.99775 |
| R-Square (COD) | 0.9955 |
| Adj. R-Square | 0.99325 |

| Specimen | 20% PS |
|---|---|
| Equation | y = a + b*x |
| Intercept | 0 |
| Slope | 1.02746 ± 0.03328 |
| Residual Sum of Squares | 0.12351 |
| Pearson's r | 0.99843 |
| R-Square (COD) | 0.99686 |
| Adj. R-Square | 0.99582 |

| Specimen | 40% PS |
|---|---|
| Equation | y = a + b*x |
| Intercept | 0 |
| Slope | 0.75109 ± 0.03059 |
| Residual Sum of Squares | 0.10431 |
| Pearson's r | 0.99752 |
| R-Square (COD) | 0.99505 |
| Adj. R-Square | 0.9934 |

| Specimen | 60% PS |
|---|---|
| Equation | y = a + b*x |
| Intercept | 0 |
| Slope | 0.46904 ± 0.01139 |
| Residual Sum of Squares | 0.01447 |
| Pearson's r | 0.99912 |
| R-Square (COD) | 0.99823 |
| Adj. R-Square | 0.99764 |

| Specimen | 72% PS |
|---|---|
| Equation | y = a + b*x |
| Intercept | 0 |
| Slope | 0.55359 ± 0.02559 |
| Residual Sum of Squares | 0.02052 |
| Pearson's r | 0.99787 |
| R-Square (COD) | 0.99574 |
| Adj. R-Square | 0.99362 |

**Figure 31:** Linear fits of initial segments of moisture uptake curves.

As can be seen, equilibrium moisture uptake decreases with increasing PS composition. This is expected given the hydrophobicity of PS and indicated that PA6 moisture resistance is improved by the addition of PS grafts. This can be exploited to mitigate challenges given by the nature of PA6 to plasticize from moisture absorption as well as hydrolytically degrade. Additionally, tailoring the hydrophobicity can allow for the creation of filtration membranes for selective separation processes.[62]

### 3.3.7 Measurement of Grafting Molecular Weight

The PS grafting molecular weight dependance on polymerization temperature was also studied. Grafting polymerizations of styrene onto PA6 were performed at 115°C and 130°C. Because these graft copolymers will not dissolve in solvents required for typical molecular weight characterization methods, fabricated specimens were hydrolyzed in superheated water to isolate the PS. The remaining PS was then soluble in common solvents such as chloroform and toluene. End-group analyses from $^{1}$H NMR in chloroform-$d_1$ and traces from GPC in THF were used to determine the PS molecular weight. Results were compared to theoretical calculations from the free radical chain growth rate expression, where temperature-dependent rate constants were calculated from the Arrhenius equation.[61] Spectra are shown in Figure 32 and results are tabulated in Table XVII.

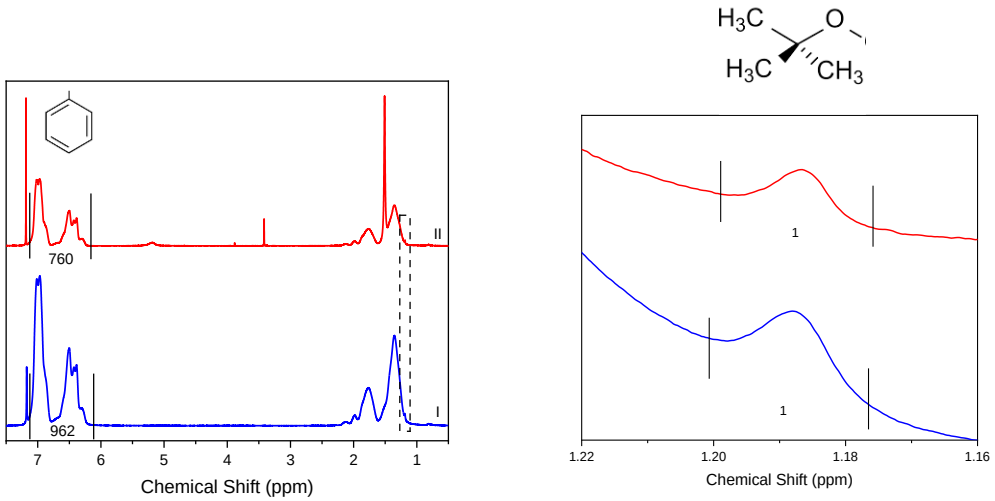


**Figure 32:** $^{1}$H NMR in chloroform-$d_1$. Peak integrals corresponding to the aromatic protons in PS (6-7 ppm) and the t-butyl protons from the TBPB initiator (1.19 ppm) used for end-group analyses are shown.

**Table XVII:** Grafting molecular weight results compared with theoretically calculated values.

| Specimen | Polymerization Temperature (°C) | Theoretical $\bar{M}_n$ (kDa) | NMR $\bar{M}_n$ (kDa) |
|---|---|---|---|
| I | 115 | 79 | 86 |
| II | 130 | 43 | 68 |

As can be seen, grafting molecular weight displays the same trend as calculated values.

GPC traces of these specimens are shown in Figure 33 and molecular weight results are tabulated in Table XVIII.

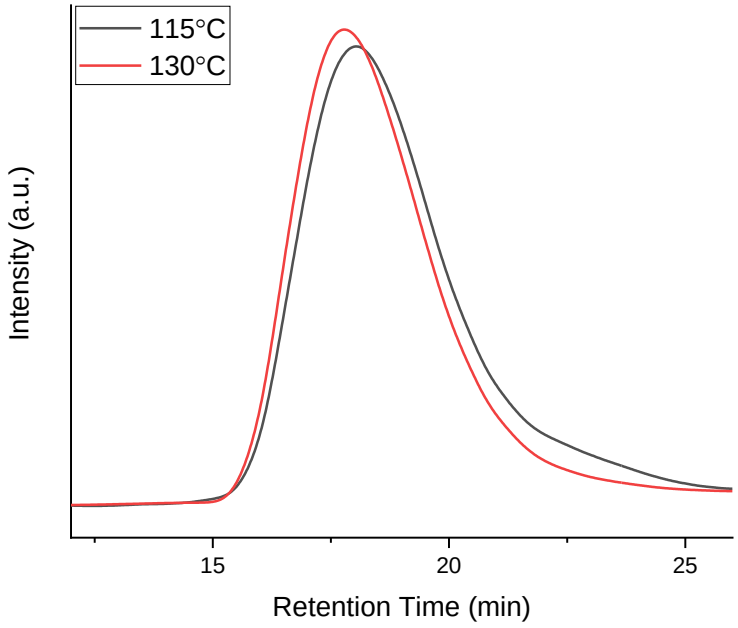


**Figure 33:** Intensity versus retention time measured by GPC in THF.

**Table XVIII:** Molecular weight results calculated from GPC traces.

| Specimen | Polymerization Temperature (°C) | $\bar{M}_n$ (kDa) | $\bar{M}_w$ (kDa) | PDI |
|---|---|---|---|---|
| I | 115 | 183 | 335 | 1.83 |
| II | 130 | 187 | 368 | 1.97 |

As can be seen, molecular weight results from GPC are approximately double than that of NMR and do not show a significant dependance on polymerization temperature. It should be noted that the NMR results were based on the assumption that two end groups from the TBPB initiator are incorporated in each PS chain. However, if termination occurred by

coupling of a PS graft with a propagating PS chain in solution, only one initiator end group per PS chain would be present. Other possible termination mechanisms include combination between neighboring grafted PS chains of the same PA6 backbone (intrachain coupling) as well as different PA6 backbones (interchain coupling), neither of which would incorporate the initiator as an end group. Given this, the GPC results are suspected to be a more accurate representation of the true grafting molecular weight, indicating that polymerization temperature did not play a large role.

### 3.3.8 Incorporating Hydrophilicity in PA6

In addition to styrene, another monomer, diethylene glycol methyl ether methacrylate ($MEO_2MA$), was polymerized in PA6. In contrast to PS, P($MEO_2MA$) is hydrophilic and can potentially be useful when added to PA6 for filtration applications.[63] Swelling experiments on this specimen was performed by immersion in water at room temperature. Results in comparison to unmodified PA6 are shown in Figure 34.

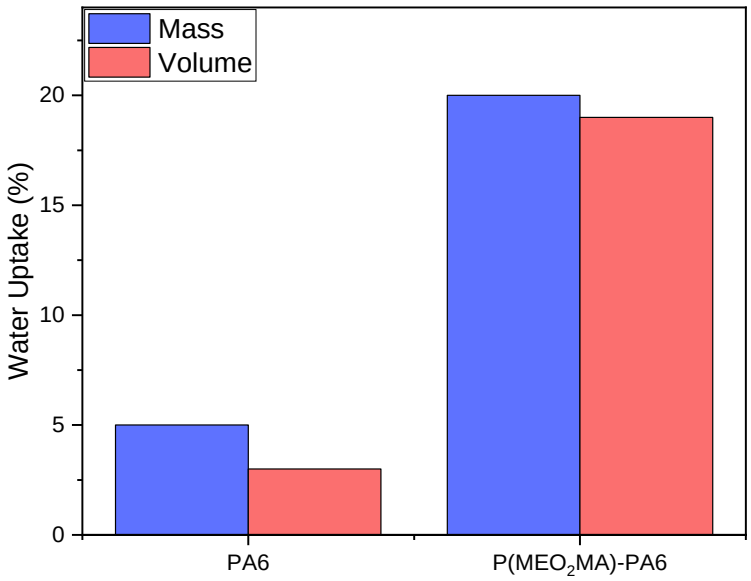


**Figure 34:** Water Uptake of P($MEO_2$MA)-PA6. The composition of this specimen was 13 wt % P($MEO_2$MA).

As can be seen, both mass and volume increases are approximately 300% compared to unmodified PA6. This shows the wide range of properties that can be achieved by grafting various polymers onto PA6.

## 3.4 Conclusions

Supercritical $CO_2$ was effective at incorporating PS into semi-crystalline polymers of various geometries without modifying the crystalline phase. Through detailed extraction procedures, removal of the PS homopolymer from modified specimens was achieved and grafting was elucidated. Both DSC and ssNMR were used to calculate graft yields and

showed consistent trends. Mean graft yield results were 98% for PA6, 59% for PET, and 15% for iPP, following the same hierarchy as the free radical stability of each polymer.

Due to the incredible yield, further investigations were performed on PA6 specimens and many useful property achievements were observed. These graft copolymers appeared to be high-$T_g$, re-meltable materials with improved moisture resistance. Finally, it has been shown that this technique is versatile as the grafting polymer can be changed to tune the final properties of the overall copolymer. One can imagine, then, tuning the graft density and molecular weight to exhibit interaction parameters needed to act as an impact modifier or compatibilizer. This opens a new route to upcycling as many potential uses were found by grafting to this engineering plastic, one of which can be applied in compatibilizing waste streams.

We anticipate that this concept can be used to synthesize a broad range of semi-crystalline copolymers where truly unique materials will result simply from the inherent crystal structure of the polymeric backbone. In turn, this can lead to a new class of compatibilizers, impact modifiers, and other materials whose morphologies could not be generated using more traditional synthetic routes. This cost-effective, sustainable process can be applied in upcycling semi-crystalline plastics, avoiding degradation of material that would normally occur during common recycling processes.

# CHAPTER 4

# EVALUATION OF ADHESION MECHANISMS IN FRONTALLY POLYMERIZABLE ADHESIVES

## 4.1 Introduction

Frontal polymerization (FP) is a self-propagating reaction which generates a spatially propagating, localized reaction zone.[64] Depending on the type of the front driving the propagation, FP is classified as follows: 1) thermal, where propagation is driven by the exotherm released during polymerization,[65] 2) photo, where the polymerization is driven by a constant UV source,[66] and 3) isothermal, which relies on the Norrish-Trommsdorff gel effect.[67]

Among these, thermal FP shows the most versatility of materials available and fastest achievable front velocities. Fronts of this nature are self-sufficient to polymerize following point initiation without the use of additional external energy.[64] Many different classes of polymer materials have been prepared by thermal FP such as addition curing of polyurethanes,[68] free radical polymerization of acrylates,[65] anionic polymerization of caprolactam,[69] and cationic polymerizations.[70,71] One example of interest is radical-induced cationic frontal polymerization (RICFP) of epoxide monomers. The production of high-$T_g$, high-performance thermosets utilizing this technique is desirable due to its cost-effective, sustainable nature compared to conventional curing methods, where external heat sources and/or volatile organic compounds (VOCs) are required.[72]

Although many studies have dealt with epoxy RICFP[70,71,73–75] there remain unsolved challenges for practical applications. One major challenge is the ability to sustain a propagating front in configurations where interfaces are buried and/or resin thickness is limited. This is needed for example when relying on FP of resin to adhere two surfaces. Although FP is particularly advantageous for adhesives by providing the ability to be cured on demand, heat loss from the reaction to the surroundings becomes a limiting factor in achieving full front propagation.[76]

Accordingly, the scope of FP adhesive applicability has been limited to a small range of materials and configurations. Holt and Pojman[77] demonstrated the use of frontally polymerizable acrylates as adhesives in 2016, but only reported successful adhesion to wood. Wigdorski[78] patented a cationically curable film adhesive that can be UV initiated and oven-cured but was not reactive enough to frontally polymerize. Even when oven-cured, adhesion was only reported for steel and fiberglass-reinforced epoxy. As a result, the practical use of frontally polymerized adhesives has been limited to selective applications; i.e. fastening steel tie bars in reinforced concrete fabrication.[76,79]

Herein, we present an epoxy formulation that undergoes FP effectively through buried interfaces and provides adhesion to a broad class of materials. This formulation is evaluated for FP in the context of three configurations where varying material properties contacting the resin are investigated. These configurations are 1) resin confined between buried substrate interfaces, 2) within test tubes immersed with metallic wire, and 3) free-standing resin droplets on substrates. The effect of boundary conditions not only from a geometric point of view, but also a material properties point of view, on FP and adhesion

is investigated. Buried interfaces and wire cured specimens allow for lap shear and pull-out testing, respectively, of adhered material. However, new challenges and limitations arise while utilizing this formulation. First, the heat release from excessive exothermic energy can cause one or more of the components in the formulation to volatilize during FP, creating defects in the adhesive joint. This is not only detrimental to the adhesive strength, but also renders its use impractical due to the toxicity of the volatile components. We further understand this by measuring the front temperature and propagation rate at a range of resin thicknesses. Moreover, the low viscosity of this formulation renders applying the resin to substrates difficult without the use of additional confinement. Hence, further modifications of the formulation are required to create FP adhesive resins with desirable viscosity and stability. The opportunity to utilize volatilization during FP to generate porosity is also recognized and preliminarily investigated herein.

## 4.2 Materials & Methods

3,4-Epoxycyclohexylmethyl 3,4-epoxycyclohexanecarboxylate (ECC), 1,1,2,2-tetraphenyl-1,2-ethanediol (TPED), and 14 nm fumed silica nanoparticles were purchased from MilliporeSigma. Diglycidyl ether of bisphenol A (DGEBA) (DER 332) and p-(octyloxyphenyl) phenyliodonium hexafluoroantimonate ($IOC_8$ $SbF_6$) were purchased from Olin Epoxy and Gelest, respectively. Jeffamine D230 was purchased from Huntsman. Various substrates used for lap shear testing were purchased from McMaster-Carr, including polycarbonate (PC), polymethylmethacrylate (PMMA), marine-grade plywood, brass, aluminum, and steel. Copper, aluminum, and steel wires were also purchased from McMaster-Carr. Polyamide 6 (PA6), polyamide 6,6 (PA66), and polybutylene

terephthalate (PBT) substrates were provided by BASF, formulated both with and without the addition of heat stabilizers. Isotactic polypropylene (iPP) in pellet form was provided by ExxonMobil and fabricated into substrates by compression molding at 200°C for 30 minutes and then cooling in another compression molding apparatus at room temperature. Epoxy substrates were fabricated by mixing a stoichiometric amount of DGEBA and Jeffamine D230. The mixture was then poured into a mold and cured at 100°C under nitrogen for six hours. Gorilla Glue Epoxy was purchase from The Home Depot. All materials were used as received.

### 4.2.1 Resin Formulation

Resin formulations were prepared in amber scintillation vials in a stirring well as follows: The cationic initiator ($IOC_8$ $SbF_6$ and co-initiator (TPED) were added as powders to the ECC monomer and homogenized by mixing for 1 hour at 60ºC in dark conditions to minimize exposure to UV which might result in an unexpected initiation. DGEBA was then added as a second monomer and mixing was continued for another hour at 60ºC until the mixture became transparent and homogeneous. The composition of this base formulation is listed in Table XIX. In cases where the base formulation was diluted with polyol, polyol was first added to the ECC monomer prior to adding the two initiators. When modified with fumed silica, the base formulation was manually mixed with fumed silica particles. All samples were then kept in dark conditions at room temperature before testing. Frontal polymerization (FP) was initiated via UV irradiation using a Lumen Dynamics OmniCure S1500 UV source set at 50% intensity with a 250-450 nm filter.

**Table XIX:** Base resin formulation compositions

| Component | Function | Mass (wt%) |
|---|---|---|
| IOC8 SbF6 | Cationic Initiator | 2.00 |
| TPED | Co-initiator | 2.00 |
| ECC | Monomer | 57.60 |
| DGEBA | Monomer | 38.40 |

### 4.2.2 Thermal Analysis

Thermal properties of the frontally polymerized resins were analyzed by thermogravimetric analysis (TGA) and differential scanning calorimetry (DSC). TGA was performed from 30 to 800℃ at a heating rate of 10 K/min in nitrogen atmosphere. DSC thermograms were recorded from 0 to 250℃ at a heating rate of 10 K/min in nitrogen atmosphere.

### 4.2.3 Frontal Polymerization

FP was carried out in three different configurations: FP under buried interfaces for lap shear testing, in test tubes for wire pull-out testing and measuring the propagation rate and cured density, and FP of free-standing resin droplets for contact-angle measurements.

To prepare specimens for lap shear testing, two rectangular substrates were slotted into a U-shaped polytetrafluoroethylene channel with a shim to make a desired thickness of adhesive as shown in Figure 35.

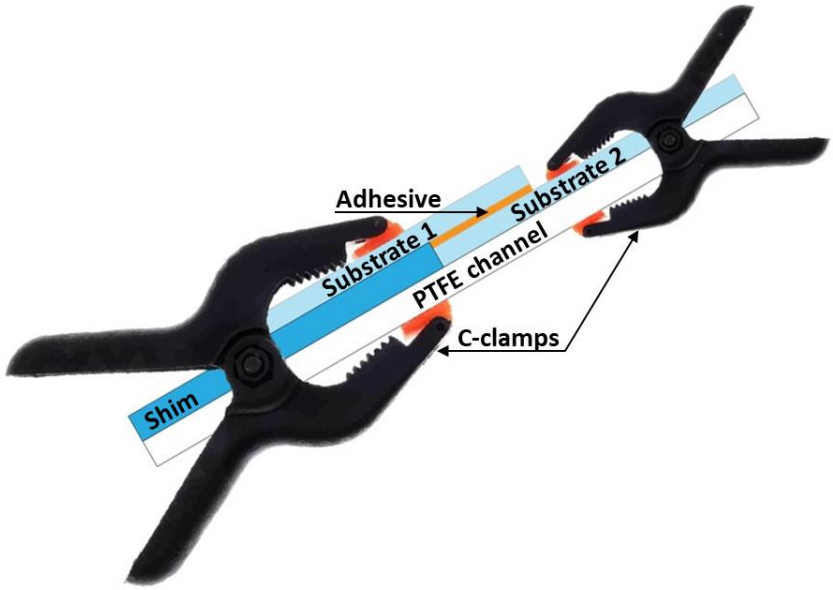


**Figure 35:** Lap shear specimen fabrication jig.

To fill the gap between two substrates with the adhesive, the sample jig was placed at an angle of approximately 45º, the adhesive was applied to the bottom substrate, and the top substrate was slowly pushed upward until the desired adhesive bond length was achieved. The substrates were tightly clamped in place to avoid displacement during FP. FP was initiated at the top corner of the sample and allowed to propagate. When FP was completed, the sample was kept undisturbed for a minimum of 10 minutes to cool to room temperature before removal from the jig. Lap shear specimens using the Gorilla Glue Epoxy adhesive were prepared with the same gap filling method. In these cases, curing was done by allowing the resin-filled samples to remain static in the jig at room temperature for 30 minutes.

Approximately 2.6 mL of resin was placed in 11 mm inner-diameter glass test tubes which were marked vertically in 15 mm increments to measure the rate of propagation. UV

was irradiated from underneath the test tube to initiate the front. Video was recorded during each polymerization where time stamps were matched as the front propagated vertically through each marking, enabling measurements of propagation rate. When FP was completed, the sample was kept undisturbed for a minimum of 10 minutes to cool to room temperature before removal from the test tubes. Once removed, bulk density measurements were performed. In cases where resin was polymerized in the presence of an immersed metallic wire, approximately 5.2 mL of resin was placed in the same test tube. To precisely control overlap length of wire in resin, Teflon tape was used to cover the metal wire above the desired exposed length as shown in Figure 36. All the other procedures were the same with the FP without metallic wires.

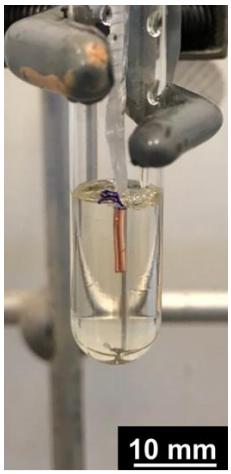


**Figure 36:** Metal wire immersed in resin before FP.

For the free-standing resin droplets, approximately 1 cm diameter resin droplets were placed on different substrates and frontally polymerized via UV initiation. The

contact angle was measured using a tensiometer for droplets both before cured and uncured droplets.

### 4.2.4 Adhesion Testing

Adhesion testing was carried out using an Instron 5500R Mechanical Tester. For lap shear specimens, testing was performed in tension with a tensile displacement rate of 1 mm/min. All substrates tested in this study were 25.4 mm in width and 76.2 mm in length, whereas the length of the adhered region and the thickness of the bond line varied. To minimize any possible offset in the axes during testing, the samples were fabricated with holes in the substrates 12.7 mm from the outer edge. The samples were attached to the Instron with cylindrical pegs having a similar diameter as the holes in the substrates. These pegs transferred the tensile load to the sample. For wire pull-out specimens, testing was performed in tension with a tensile displacement rate of 2 mm/min. Samples were attached to the Instron using grips on both the wire and surrounding resin, respectively. All samples were tested in tension until failure.

Adhesion testing to a variety of substrates was performed using a lap shear configuration where stress distributions at failure were calculated using a shear lag model.[80] This model is appropriate for the calculation of adhesives adhering to two substrates with different material properties. This allowed for configurations in all cases where one substrate was transparent and exhibited remarkable adhesion thereby promoting failure at the other material interface. Consequently, both *in-situ* monitoring of frontal polymerization as well as adhesive strength measurements of various substrates was

facilitated. A schematic of this configuration and accompanying equations of the shear lag model are outlined in Figure 37 and equations (4.1) through (4.7):

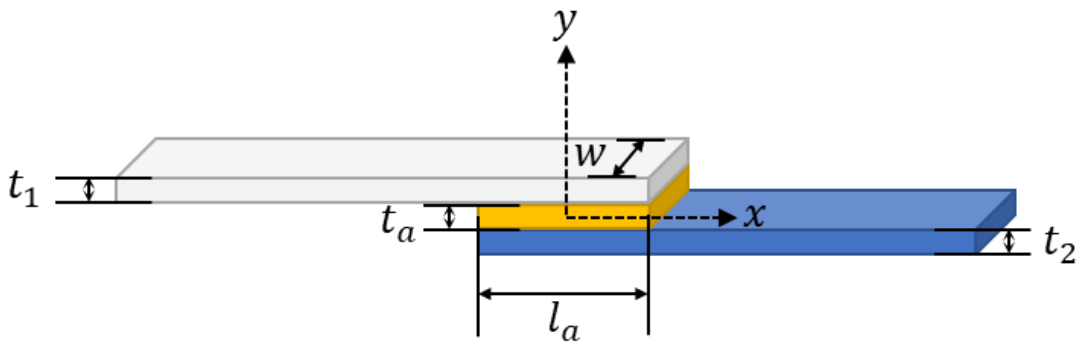


**Figure 37:** Lap shear configuration schematic.

$$\tau = C_1 \cosh(\omega\chi) + C_2 \sinh(\omega\chi) \tag{4.1}$$

$$C_1 = \frac{P\omega}{2wl}\left[\frac{1}{\sinh\left(\frac{\omega}{2}\right)}\right] \tag{4.2}$$

$$C_2 = \left(\frac{\psi-1}{\psi+1}\right)\frac{P\omega}{2wl}\left[\frac{1}{\cosh\left(\frac{\omega}{2}\right)}\right] \tag{4.3}$$

$$\omega^2 = (1+\psi)\phi \tag{4.4}$$

$$\psi = \frac{E_1 t_1}{E_2 t_2} \tag{4.5}$$

$$\phi = \frac{Gl^2}{E_1 t_1 t_a} \tag{4.6}$$

$$\chi = \frac{x}{l} \tag{4.7}$$

where P is the load at failure, l is the adhesive overlap length, $t_a$ is the adhesive thickness, G is the adhesive shear modulus, $E_{1\&2}$ are Young's moduli of substrates 1 and 2,

respectively, $t_{1\&2}$ are thicknesses of substrates 1 and 2, respectively, and W is the specimen width.

Specimens were also prepared where metal wire was immersed in resin encapsulated by a cylindrical test tube as schematically represented in Figure 38. Following polymerization, the cured resin and wire was removed from the test tube. Pull-out testing was then performed, and shear stress distributions were calculated using equation (4.8) and (4.9).[81]

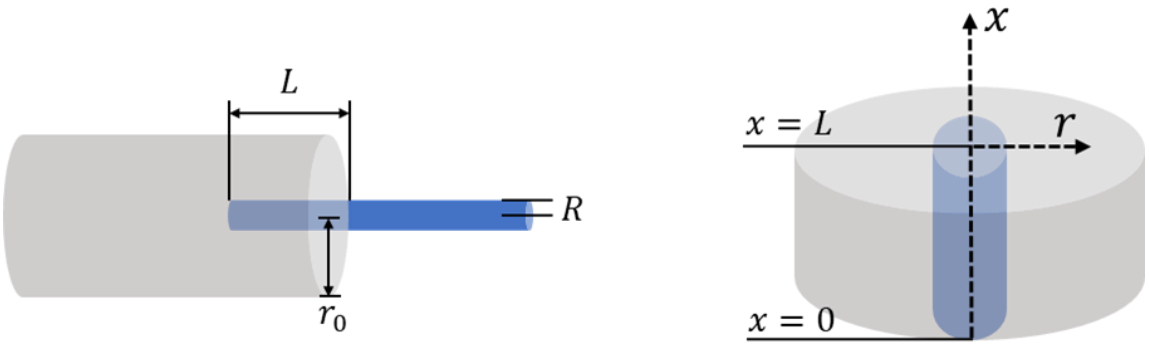


**Figure 38:** Wire pull out testing schematic.

$$\tau(x) = \frac{nP}{2\pi R^2} cosh\left(\frac{nx}{R}\right) cosech\left(\frac{nL}{R}\right) \tag{4.8}$$

$$n = \sqrt{\frac{2G_m}{E_f \, ln\left(\frac{r_0}{R}\right)}} \tag{4.9}$$

where P is the load, R is the wire radius, L is the overlap length, $r_0$ is the distance from the wire axis to the adhesive boundary, and $G_m$ is the shear modulus of the adhesive.

### 4.2.5 Resin and Adhesive Rheological Properties

The modulus of the frontal adhesive was measured using a TA instruments model Q800 Dynamic Mechanical Analyzer (DMA). Test specimens were created by frontally polymerizing resin on non-adhering surfaces. Cured resin was then cut and polished to approximately 3 mm in width and 1.5 mm thickness. Approximately 9.5 mm length was provided between grips under 0.01 N normal tensile force and a frequency of 1 Hz with 1 N amplitude. A heating rate of 3 K/min was used at a temperature range of -25°C to 200°C. The shear modulus of the Gorilla Glue Epoxy was measured using a TA instruments model AR 2000 rheometer equipped with a 25 mm diameter parallel plate fixture. Uncured resin was placed in between the plates separated by a gap height of 1.5 mm. An oscillation time sweep was applied at room temperature using an oscillatory stress of 100 Pa at 1 Hz as the resin cured *in-situ*. Viscosity of the uncured frontal resin was also measured using this setup by imposing an oscillatory shear rate sweep from 0.1 to 10 Hz.

### 4.2.6 Front Temperature Measurements

Infrared videography was used to measure the temperature during frontal polymerization *in-situ*. Standard videos were taken simultaneously where a ruler was placed in the field of view such that the propagation rate can also be measured. FP in this configuration was prepared by pouring the resin into a PDMS mold clipped to glass underneath. Varying mold thicknesses were used. Both video and infrared cameras were suspended above the mold such that horizontal FP can be monitored. Initiation was

performed using UV light. A frame of the video and infrared recording is shown in Figure 39.

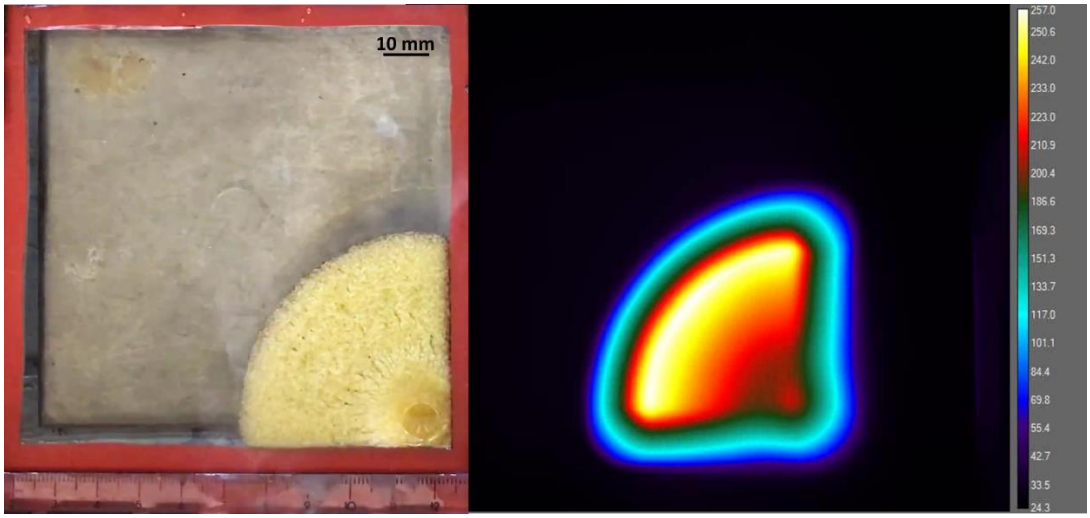


**Figure 39:** Frames of standard (left) and infrared (right) FP video recordings.

## 4.3 Results and Discussion

### 4.3.1 Thermal Analysis

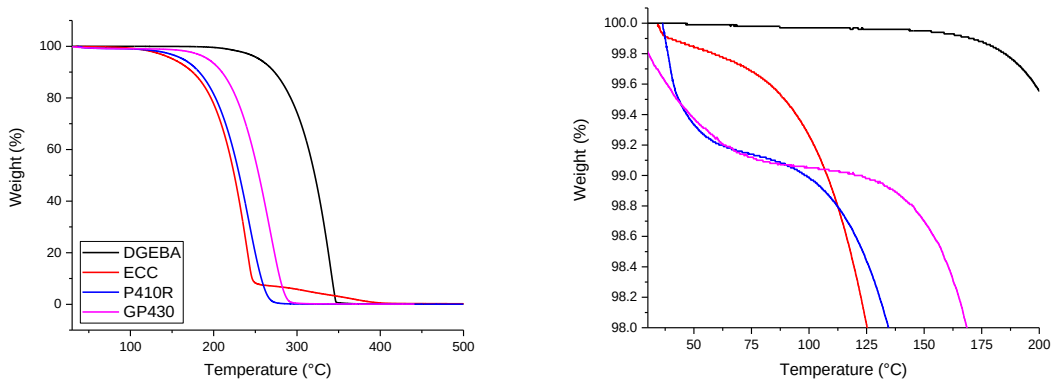


**Figure 40:** TGA of resin components. The graph on the right is magnified to display early temperature mass losses.

Figure 40 shows the TGA thermograms of resin components in a nitrogen atmosphere. Each resin component exhibits mass losses at different temperatures. Much of the ECC monomer volatilizes by 250℃ while both polyols, P410R and GP430, almost completely volatilize at around 300℃. The DGEBA monomer shows the highest thermal stability and volatilizes by 350℃. Additionally, both polyols and the ECC monomer show slight mass losses at lower temperatures, from 50-200℃ as displayed in the magnified portion of the figure.

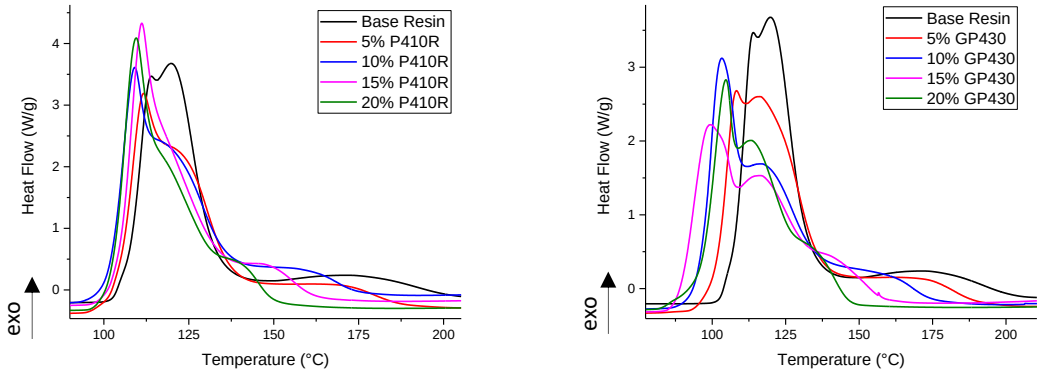


**Figure 41:** DSC of resin formulations. Left) P410R diluted formulations. Right) GP430 diluted formulations.

Figure 41 shows the DSC thermograms of different resin formulations diluted by various compositions of the polyols. Despite a very small weight loss below 150°C in TGA curves, DSC thermograms yield a notable exotherm giving maxima in between 100 and 125°C. Thus, the exothermic peak is ascribable to the heat released by the frontal polymerization. Though the temperature in FP varies with boundary conditions, these

results, in complement to TGA, can provide an estimate of whether formulation components will volatilize and generate porosity during FP. Measurements from these DSC traces are tabulated in Table XX.

**Table XX:** Effects of adding polyols P410R and GP430 to the base formulation on onset temperature of the exotherm ($T_o$), exotherm peak temperature ($T_p$), and exotherm energy based on DSC results.

| **Polyol (wt %)** | **P410R** | | | **GP430** | | |
|---|---|---|---|---|---|---|
| | $T_o$ (°C) | $T_p$ (°C) | Energy (J/g) | $T_o$ (°C) | $T_p$ (°C) | Energy (J/g) |
| 0 | 100 | 120 | 605 | 100 | 120 | 605 |
| 5 | 95 | 112 | 563 | 91 | 108 | 590 |
| 10 | 92 | 110 | 555 | 85 | 103 | 551 |
| 15 | 95 | 111 | 517 | 83 | 99 | 507 |
| 20 | 95 | 110 | 497 | 81 | 104 | 450 |

### 4.3.2 Adhesive Rheological Properties

Rheological measurements of the frontal adhesive and Gorilla Glue Epoxy adhesive are shown in Figure 42.

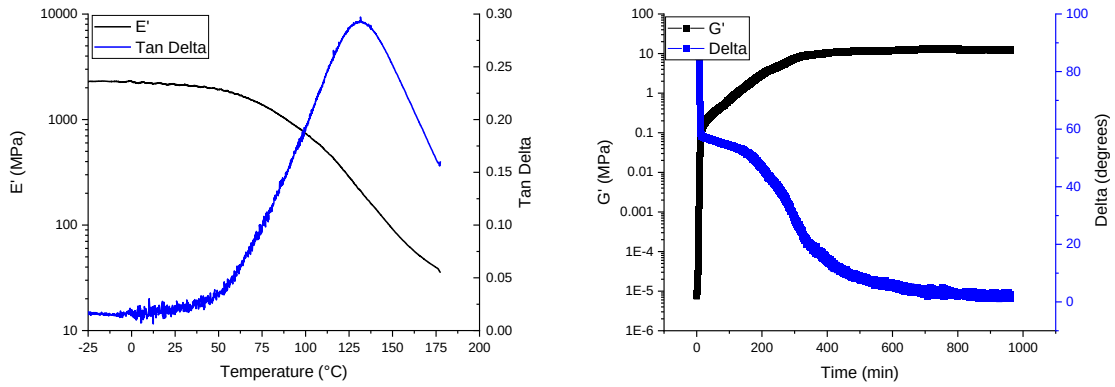


**Figure 42:** DMA trace of frontal adhesive (left) and rheology of Epoxy Gorilla Glue adhesive (right).

The storage modulus of the cured frontal adhesive at room temperature is 2300 MPa. The shear modulus was calculated using equation (4.10)

$$G = \frac{E}{2*(1+\nu)} = \frac{2300\ MPa}{2*(1+0.3)} = 880\ MPa \tag{4.10}$$

where G is the shear modulus, E is the normal tensile modulus, and ν is Poisson's ratio. As can be seen, the shear modulus of the gorilla glue adhesive increased as the resin cured and reached a steady state of 12.5 MPa at 500 min. Thus, the shear modulus values of the frontal adhesive and the Epoxy Gorilla Glue adhesive used in the shear lag calculations were 880 MPa and 12.5 MPa, respectively.

### 4.3.3 FP under Buried Interfaces

PC, due to its transparency allowed for in-situ monitoring of FP as shown in Figure 43. It was found that the minimum resin thickness requirement for PC-PC lap shear specimens to repeatedly produce a fully propagating front was 1.6 mm. After FP, the cured resin adhered to both PC substrates.

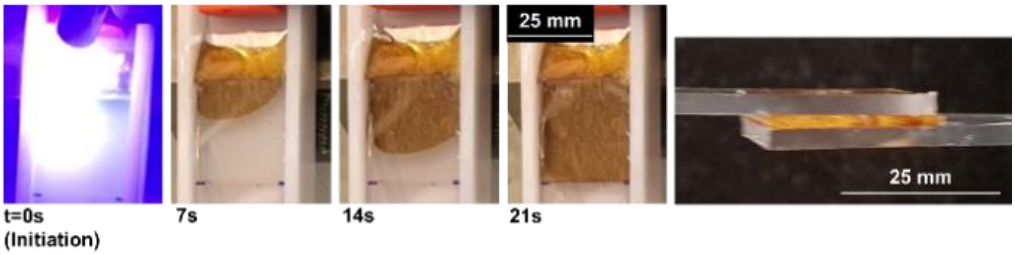


**Figure 43:** Frontal polymerization between two PC substrates (left). Side-view of fabricated specimen after FP (right).

Following this study, a constant 1.6 mm thickness was applied to all remaining substrates. FP was performed on these substrates in an asymmetric fashion where PC was used as the transparent, upper substrate to monitor FP while the opposing substrate varied. In addition to PC, full propagation and adhesion was observed for PBT, PBT with heat stabilizers, PMMA, iPP, and plywood. Lap shear testing was performed on adhered substrates utilizing the shear lag model (Figure 37) to accommodate opposing substrates of different material properties. Results are displayed in Figure 44 and adhesive strength values are tabulated in Table XXI.

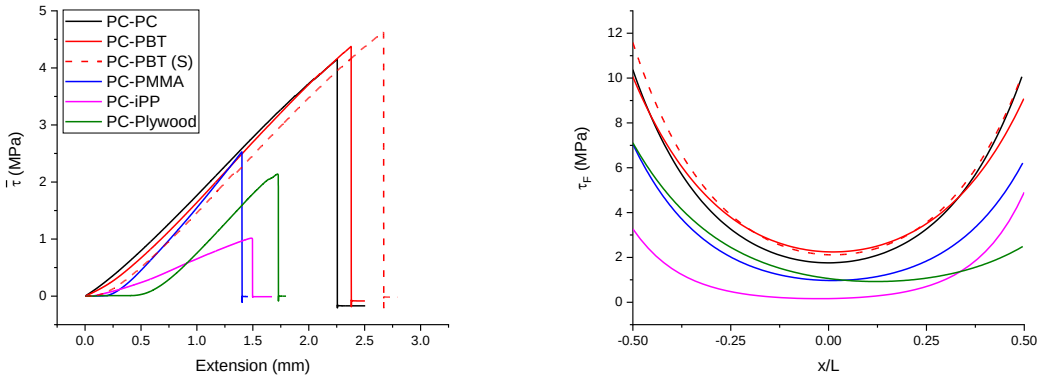


**Figure 44:** Average shear stress versus extension (left) and shear lag stress distributions along the adhesive upon failure (right). "(S)" denotes substrates which contain heat stabilizers.

**Table XXI:** Adhesive strength values. $\bar{\tau}$ and $\tau_{Max}$ are the average and maximum shear stresses at failure, respectively. The asterisk denotes that failure occurred at the substrate rather than the adhesive, indicating a lower bound value for adhesive strength. "(S)" denotes substrates which contain heat stabilizers.

| **Substrates** | **$\bar{\tau}$ (MPa)** | **$\tau_{Max}$ (MPa)** | **$\tau_{Max}/\bar{\tau}$** |
|---|---|---|---|
| PC-PC* | 4.61 ± 0.73 | 11.04 ± 0.68 | 2.39 |
| PC-PBT* | 4.38 ± 0.00 | 10.03 ± 0.03 | 2.29 |
| PC-PBT (S)* | 4.72 ± 0.07 | 11.65 ± 0.05 | 2.47 |
| PC-PMMA | 2.41 ± 0.08 | 6.73 ± 0.23 | 2.79 |
| PC-iPP | 1.03 ± 0.01 | 5.25 ± 0.24 | 5.10 |
| PC-Plywood | 2.08 ± 0.03 | 6.93 ± 0.09 | 3.33 |
| PC-Polyamide | No adhesion | | |
| PC-Polyamide (S) | No adhesion | | |
| PC-Epoxy | No adhesion | | |
| PC-Metal | No adhesion | | |

The strongest adhesion was observed for PC-PC, PC-PBT, and PC-PBT (S). In these cases, the adhesive did not fail. Rather, one of the two substrates fractured at a region slightly beyond the overlap length where the adhesive was applied (Figure 45). Therefore,

measured values resemble the strength of the substrate rather than the adhesive. It was observed that PC-PBT (S) specimens failed at the PC substrate while PC-PBT specimens failed at the PBT substrate. This is most likely because PBT is weaker than PBT (S) due to chain scission during the substrate fabrication process. Thus, the measured adhesive strength values for PC-PBT (S) specimens are larger than PC-PBT and statistically equivalent to the symmetric case where PC was used for both interfaces. This simply indicates that the PC used in this study was stronger than PBT but weaker than PBT (S). It does not appear, however, that stabilizers had any effect on the actual adhesion.

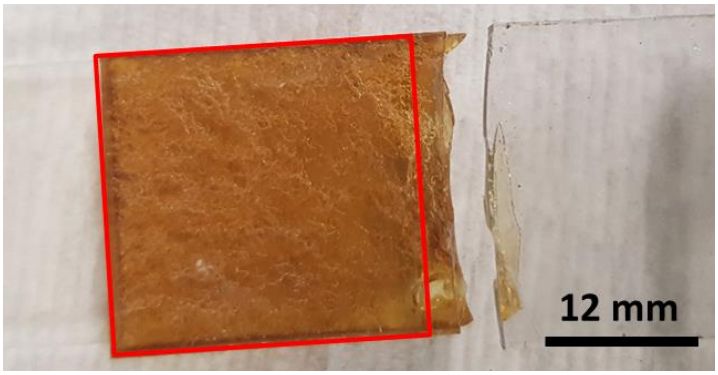


**Figure 45:** PC substrate after failure. The red box encompasses the overlap region where the adhesive was applied between both substrates.

Over the broader range of materials tested, however, it is unclear why adhesive strength varies depending on the applied substrate. It is possible that in some cases, melting or deformation of interfaces due to heat release from the front causes *in-situ* local mixing with the adhesive as curing occurs. The strong adhesion to PC and PBT can additionally result from aromatic π stacking between the adhesive and substrate.

Adhesion was not observed for PC-polyamide (PA6 and PA66), PC-polyamide (S), PC-epoxy, and PC-metal (aluminum, brass, and steel). In these cases, frontal polymerization proceeded fully throughout the length and width only at the interface of the PC substrate. At the interface opposing the PC substrate, however, a thin layer of liquid resin remained and easily delaminated from the solidified portion. This is depicted in the PC-polyamide specimens in Figure 46. Similar to PBT, the presence of heat stabilizers in polyamides did not affect adhesion or the curing behavior of the frontal resin.

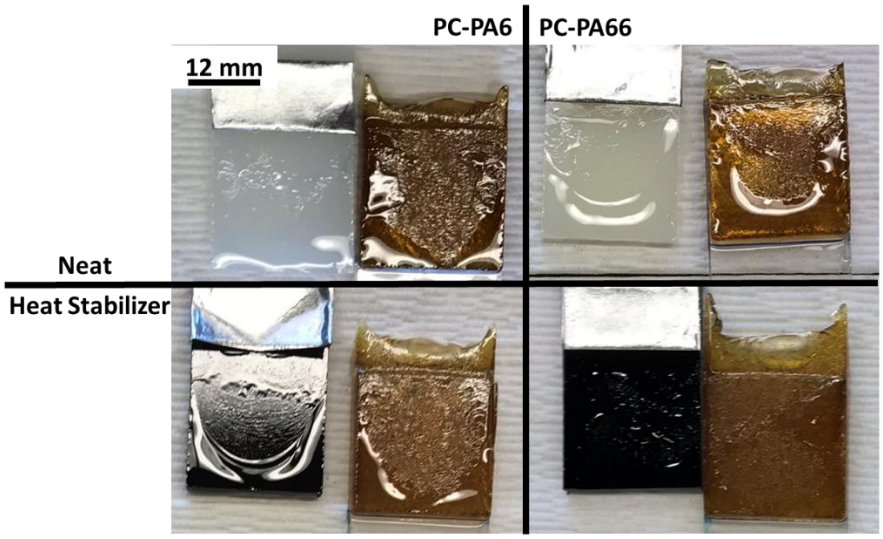


**Figure 46:** PC-Polyamide substrates after frontal polymerization.

This residual resin was tested via FTIR and compared with both the base resin and solidified adhesive. Spectra are shown in Figure 47.

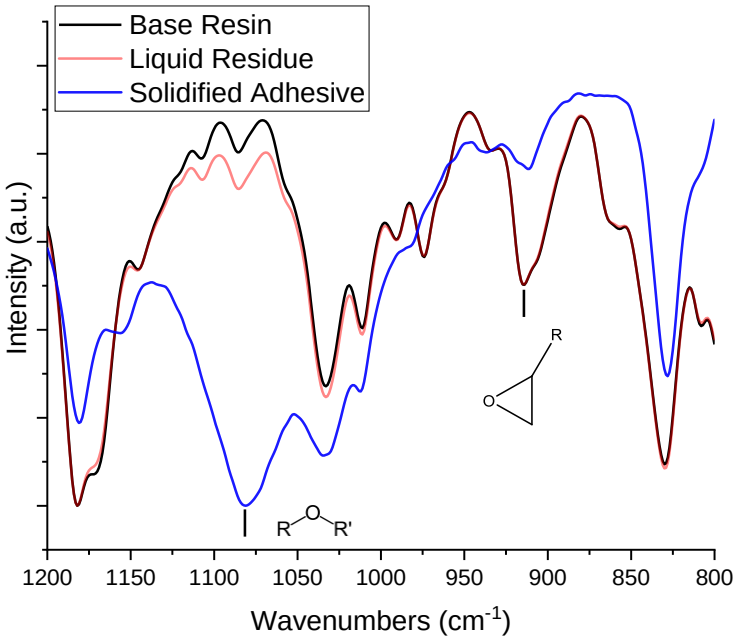


**Figure 47:** FTIR results of base resin, residual liquid after FP, and the solidified adhesive.

Both the base resin and liquid residue show a pronounced epoxide peak at 920 $cm^{-1}$, indicating that the monomers did not polymerize. This verifies that the residual resin leftover at unadhered substrate interfaces remained uncured. In contrast, the solidified adhesive shows a minuscule epoxide peak and a pronounced ether peak at 1080 $cm^{-1}$ resulting from the epoxy ring opening. The observation of the unreacted layer in some substrates can be attributed to many factors. First, in case of metallic substrates, their high thermal conductivity may have dissipated sufficient heat from the moving reaction front, causing extinction.[82] This explanation does not, however, make clear why some polymeric

substrates also showed this layer of uncured resin. The effect of stabilizers has already been ruled out. However, the commonality between the unadhered polymeric substrates is the presence of nitrogen moieties. It is possible then, that in the case of PA and epoxy substrates, the nitrogen moieties acted as radical scavengers during the FP process, inhibiting the radically promoted front.

The gorilla glue epoxy adhesive was tested on PC-iPP. Results are shown in Figure 48 and tabulated in Table XXII.

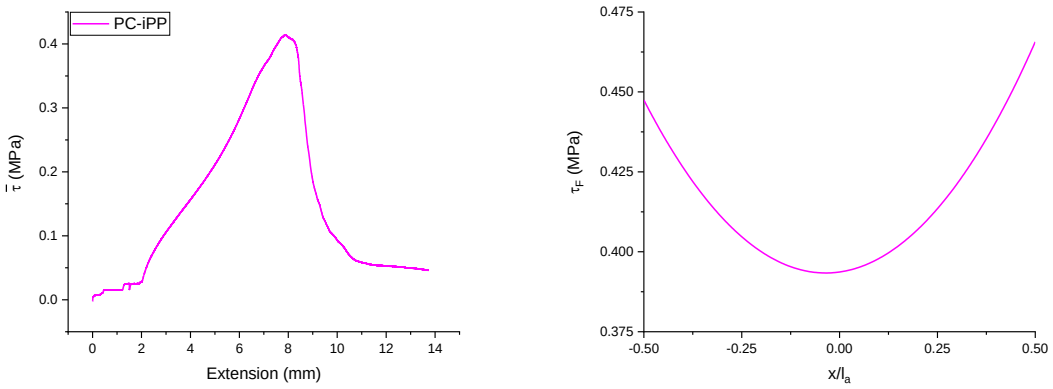


**Figure 48:** Average shear stress versus extension (left) and shear lag stress distribution along the length of the adhesive upon failure (right) for the Gorilla Glue Epoxy adhesive.

**Table XXII:** Adhesive strength values for the Gorilla Glue Epoxy adhesive. $\bar{\tau}$ and $\tau_{Max}$ are the average and maximum shear stresses at failure, respectively.

| Substrates | $\bar{\tau}$ (MPa) | $\tau_{Max}$ (MPa) | $\tau_{Max}/\bar{\tau}$ |
|---|---|---|---|
| PC-iPP | 0.28 ± 0.09 | 0.32 ± 0.11 | 1.14 |

As can be seen, the adhesive strength from this commercial adhesive to iPP is approximately an order of magnitude lower than the frontal adhesive generated from the base resin.

### 4.3.4 FP in Test Tubes

FP was performed on resin in test tubes surrounding immersed metal wire. Initiation was done through the bottom of the test tube such that steady-state front propagation was reached before contacting the metal. Additionally, a larger volume of resin was used relative to contact area with the metal in contrast to the lap shear configuration. Because of this, relative heat loss to the metal was less significant. Accordingly, adhesion was achieved to copper, aluminum, and steel wires. Pull-out testing was then performed. Pull-out results are depicted in Figure 49 and adhesive strength values are tabulated in Table XXIII. Adhesion in this case further supports the assertion that the larger thermal conductivity of metals relative to polymeric substrates was responsible for lack of curing and adhesion during FP in the lap shear configuration.

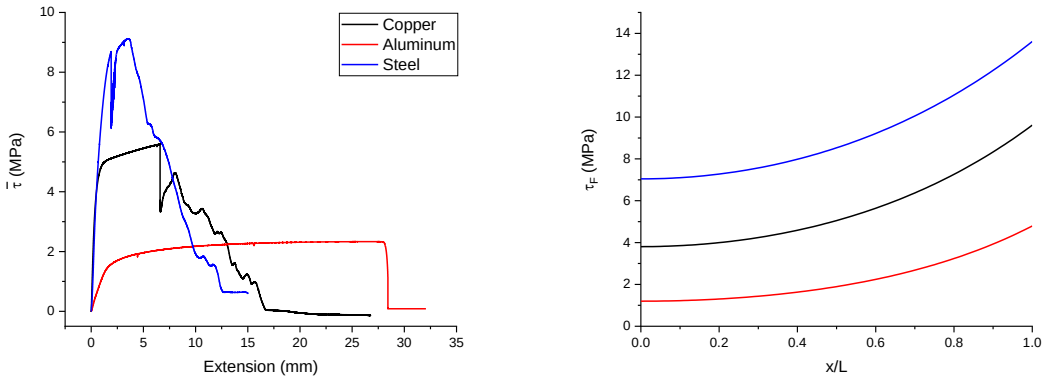


**Figure 49:** Wire pull-out shear stress versus extension results.

**Table XXIII:** Adhesive strength values corresponding to the maximum shear stresses from wire pull-out testing.

| Wire | $\bar{\tau}$ (MPa) | $\tau_{Max}$ (MPa) | $\tau_{Max}/\bar{\tau}$ |
|---|---|---|---|
| Copper | 5.67 ± 0.19 | 9.76 ± 0.33 | 1.72 |
| Aluminum | 2.24 ± 0.05 | 4.77 ± 0.10 | 2.13 |
| Steel | 8.93 ± 0.83 | 13.38 ± 1.24 | 1.50 |

### 4.3.5 FP of Free-Standing Droplets

FP was performed of free-standing resin droplets on various substrates. Contact angle of droplets before and after curing was measured to investigate differences in resin affinity. As shown in Figure 50, the lowest contact angles in pre-cured droplets were observed for the PC and epoxy substrates, indicating the highest resin affinity on these substrates. In contrast, aluminum displayed the highest contact angle indicating the lowest resin affinity while iPP has an intermediate contact angle. More statistical variations were observed for post-cured droplets but were not significantly different from pre-cured measurements.

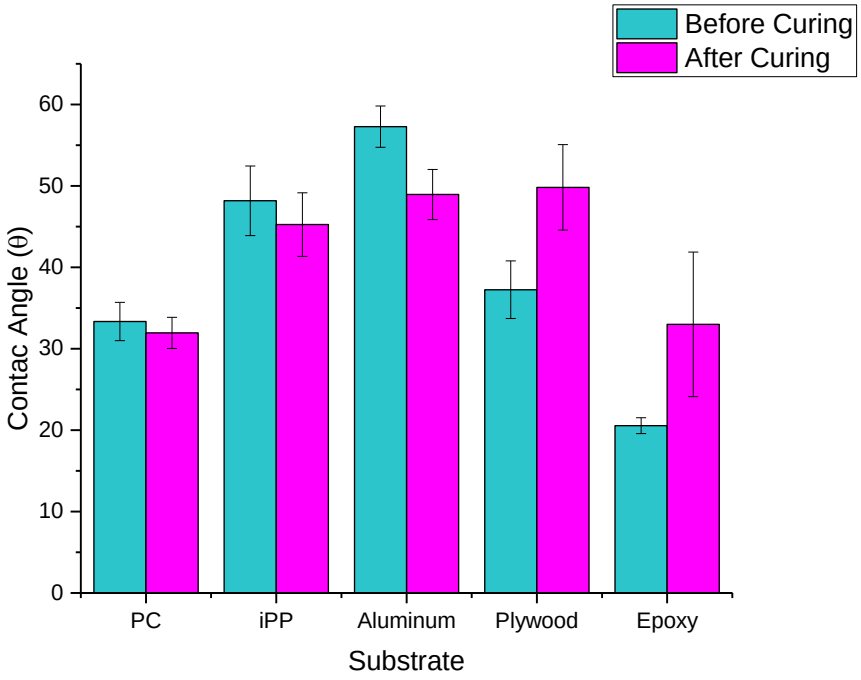


**Figure 50:** Contact angle measurements of resin droplets on substrates.

FP was successful of all droplets regardless of the underlying substrate. Following FP, all substrates displayed qualitative adhesion to the cured resin except for the epoxy substrate, where the droplet readily delaminated. This was unexpected given the low contact angle result compared to the other substrates. However, this result is similar to the lap shear case where adhesion did not occur, further asserting that the nitrogen moieties prevented FP from occurring at the interface. It is noteworthy that the cured droplets adhered well to aluminum despite the higher contact angle, whereas no adhesion to metals was observed in the lap shear configuration. It is possible that in the droplet case, FP is less likely driven by heat but more by the attenuation of UV light through transparent resin droplets. Given these factors, resin affinity appeared to be an insufficient metric in predicting adhesion in this configuration.

### 4.3.6 Propagation Rate and Density Measurements

FP in test tubes was performed to measure the front propagation rate. Density measurements of cured specimens were then conducted. Figure 51 shows snapshots during FP of the base resin.


**Figure 51:** FP of the base resin in a glass test tube. The markers were placed in 15mm increments such that propagation rate can be measured.

Initially, resin was filled to the top red marking. During front propagation, volatiles formed and traveled vertically upward above the cured resin. As this occurred, the height of the resin increased, indicating that porosity was caused by volatile formation during FP. Upon recognizing that foams can be created by FP, the base resin formulation was systematically modified with two BASF polyols to investigate the feasibility of controlling foam properties.

It can be postulated that foam properties are influenced by factors that form and entrain volatiles during FP. Measurable indications of this behavior include thermal stability of formulation components, exothermic energy, and front propagation rate. The effects of polyol concentration and exothermic energy on front propagation rate were investigated. It should be noted that both polyols have a molecular weight of 400 g/mol. However, P410R and GP430 are difunctional and trifunctional, respectively. Propagation rates versus polyol concentration and energy released measured by DSC are shown in Figure 52.

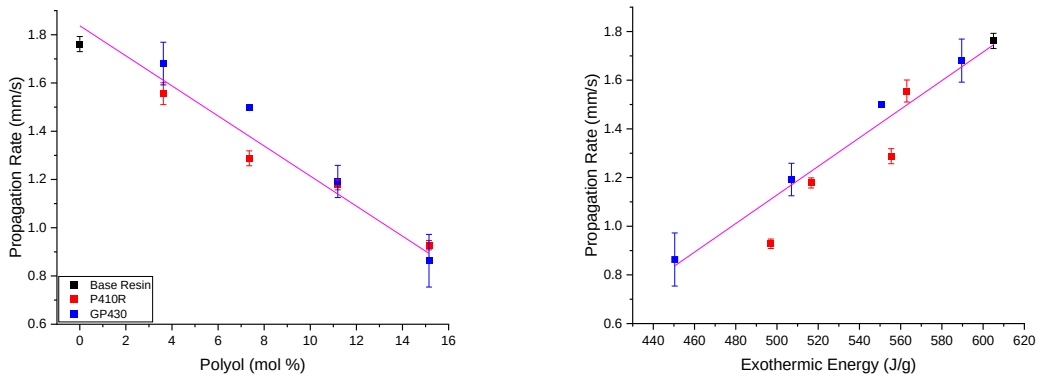


**Figure 52:** Left) propagation rate versus polyol concentration. Right) propagation rate versus exothermic energy as measured by DSC. Results corresponding to the undiluted base resin are marked in black. The data were fit to linear regressions as shown by the magenta trendlines.

Details of each linear regression are shown in Table XXIV.

**Table XXIV:** Linear fits of propagation rate versus polyol concentration and propagation rate versus exothermic energy.

| **Plot** | **Propagation Rate (mm/s) versus Polyol (mol %)** | **Propagation Rate (mm/s) versus Exothermic Energy (J/g)** |
|---|---|---|
| Slope | -6.23E-2 ± 4.4E-3 | 5.87E-3 ± 4.89E-4 |
| Intercept | 1.84 ± 0.04 | -1.81 ± 0.26 |
| $R^2$ | 0.97 | 0.96 |

The results show a linear decreasing trend in propagation rate with increasing polyol composition. The rates appear to be independent of polyol functionality as propagation rates for each polyol are statistically similar at nearly all concentrations. This indicates that the polyols are acting as a nonreactive diluent rather than participating in the polymerization chemistry. Additionally, propagation rate increased linearly with

exothermic energy. This is expected as FP kinetics are driven by the energy release during cationic ring-opening.

The effects of polyol composition and propagation rate on the foam density are shown in Figure 53.

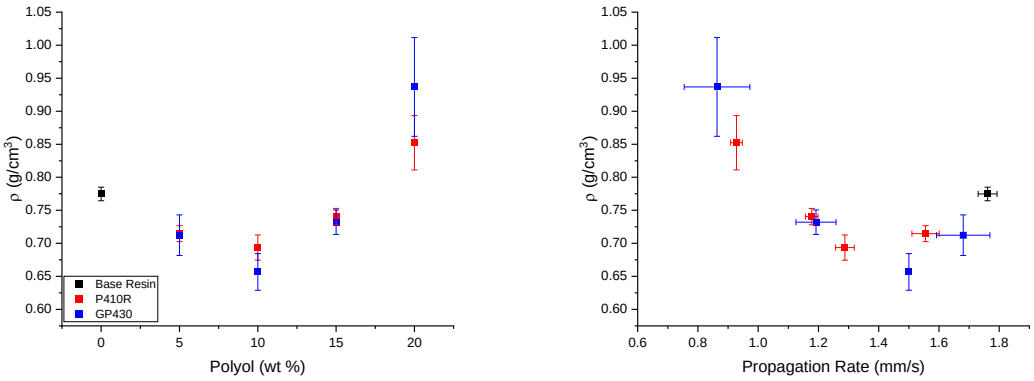


**Figure 53:** Left) density versus polyol concentration (wt %). Right) density versus propagation rate.

Density was statistically similar for lower polyol dilutions but displayed an increasing trend above 10 wt%. In this concentration range, it was also observed that density decreased with increasing front propagation rate. As shown by TGA, ECC fully volatilizes at lower temperatures than the remaining components. Consequently, the lower porosity at the higher polyol concentration may be explained, in part, simply due to the dilution of ECC, as the formulation becomes less exothermic and less volatiles are formed. However, porosity can be affected by many other factors such as resin viscosity, surface tension, vapor density, etc. that have yet to be investigated.

### 4.3.7 Formulation Modifications

14 nm fumed silica particles were added to the adhesive resin in concentrations of 5, 7.5, and 10 wt %. Resin viscosity was measured in a rheometer using a parallel plate fixture. Results are plotted in Figure 54. Zero shear viscosities were found by extrapolating the initial equilibrated viscosity values to 0 Hz. These results are tabulated in Table XXV.

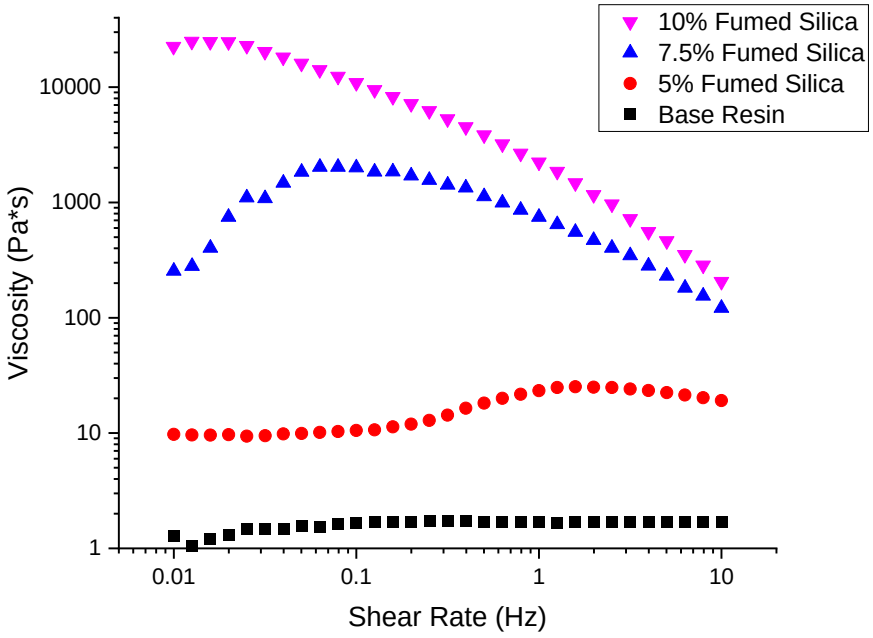


**Figure 54:** Viscosity versus shear rate of silica modified resin formulations.

**Table XXV:** Zero-shear viscosity measurements of silica modified resin formulations.

| Resin | Zero Shear Viscosity (Pa*s) |
|---|---|
| Standard | 1.70 |
| 5% Fumed Silica | 9.60 |
| 7.5% Fumed Silica | 1700 |
| 10% Fumed Silica | 24700 |

The incorporation of fumed silica dramatically increased the resin viscosity, forming a "paste-like" adhesive. In contrast to the standard resin, the silica-modified resins demonstrate more practicality as confinement is not required when applying the resin between interfaces. Lap shear adhesion testing was performed between two PC substrates using the resin with 5% fumed silica. Frontal polymerization was successful under the buried interfaces and substrate failure was observed, indicating that the additive did not negatively impact the adhesive strength.

It was also observed that volatile formation during frontal polymerization of the modified resins was drastically reduced in comparison to the base resin. This is commenserate with the decrease in front propagation rate and increase in foam density as can be seen in Figure 55. Fumed silica dilutions above 5 wt % could not be measured due to entrained air which could not escape the resin before FP due to the high viscosity.

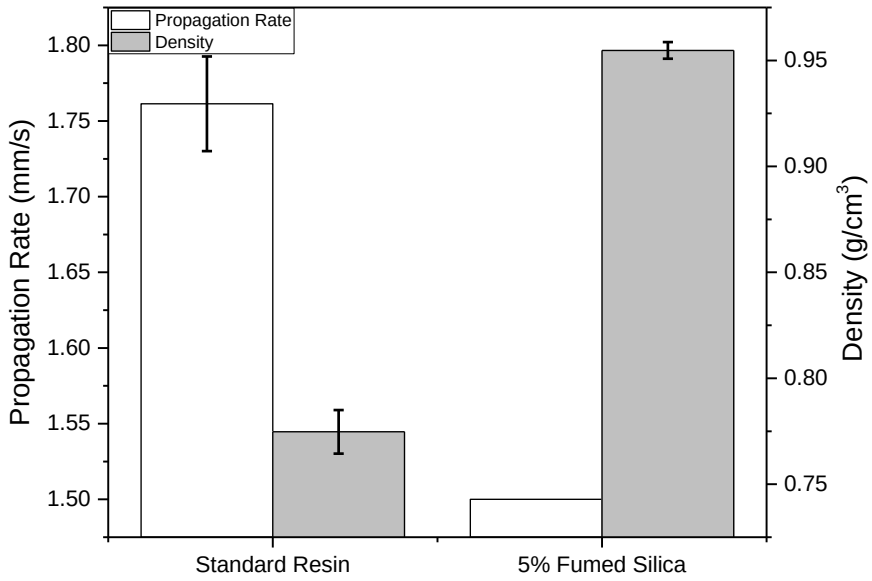


**Figure 55:** Propagation rate and density results of the standard resin and the resin with 5% fumed silica.

These results agree well with the studies done where the base formulation was diluted with polyols. As a consequence, higher foam densities are observed with slower propagating formulations where heat release during FP is reduced.

### 4.3.8 Front Temperature Measurements

As discussed previously, boundary conditions influence curing and adhesion in FP. In configurations where resin volume is limited, heat dissipation becomes significant such that a propagating front cannot be sustained. Accordingly, front temperature and propagation rate are also affected as they are directly related to heat release that occurs during FP. Quantifying this behavior is essential not only for understanding the boundary

condition limitations of a given formulation, but also for elucidating whether formulation components will volatilize. Thus, a study was performed using the base resin, where resin thickness was systematically altered. The resulting front temperatures and propagation rates were measured.

Infrared videography was used to measure the frontal polymerization temperature as propagation occurred at varying resin thicknesses. Realtime video was also taken, which allowed for propagation rate measurements. The maximum front temperature and propagation rate versus resin thickness are plotted in Figure 56.

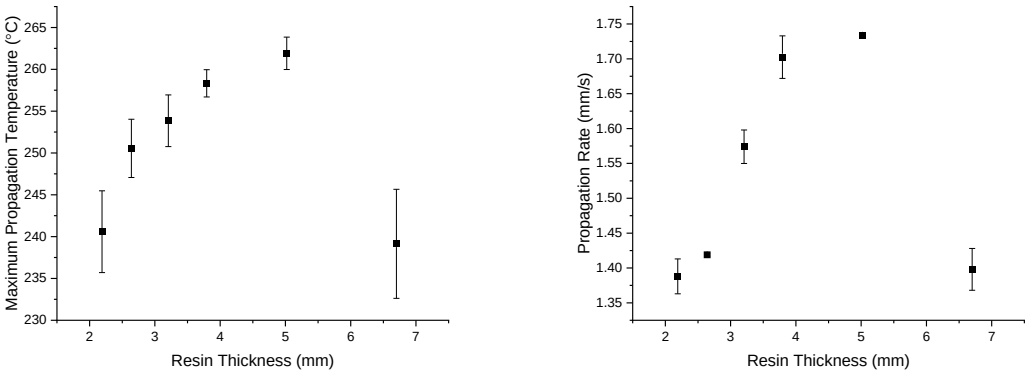


**Figure 56:** Maximum propagation temperature (left) and propagation rate (right) versus resin thickness.

As expected, both temperature and propagation rate initially increase with resin thickness because more exothermic energy is released compared to heat dissipation at the boundaries. They level off above 5 mm, which may be attributed to the dampening significance of heat loss in this larger thickness range. At 6.7 mm, however, resin thickness is large enough such that curing in the vertical direction is no longer instantaneous. Therefore, the

horizontal propagation rate and front temperature decrease due to the additional depth effect. Temperature and propagation rate are also well correlated, as shown in Figure 57.

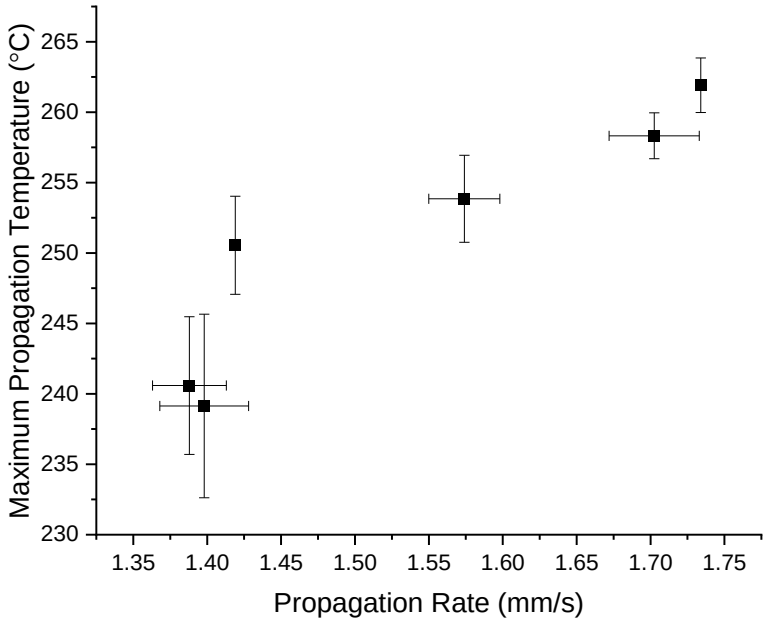


**Figure 57:** Maximum propagation temperature versus propagation rate.

This is analogous to what was shown in Figure 52, where exothermic energy and propagation rate were positively correlated in the test tube configuration. The alteration here is that the total heat release during FP was varied by changing the significance of the boundary conditions rather than the exothermic energy of the formulation. It should also be noted that front temperatures range from 240 - 265°C, which exceeds the volatilization temperature of the ECC monomer, affirming the volatilization of this component during FP. This temperature range also exceeds the melt temperature and glass transition of all

polymeric substrates tested in the lap shear configuration, enforcing that localized deformation and mixing with the adhesive may have occurred during FP.

## 4.4 Conclusions

This study showed that the frontally polymerized epoxy adhesive successfully adhered to a wide class of materials. For the case of PC-iPP, the adhesive strength was an order of magnitude larger than the commercial Gorilla Glue Epoxy adhesive. Boundary conditions proved to largely affect the strength of adhesion as well as the curing process of FP. The significance of boundary conditions was further shown by their correlation with front temperature and propagation rate. Temperature measurements in complement to TGA elucidated the volatile components in the epoxy formulation led to porosity during FP. Accordingly, these studies provide important benchmarks in assessing the limitations and uses of any frontal formulation. Modifications to the base resin enabled increasing viscosity and minimizing volatilization for adhesive applicability. Volatilization was also exploited in using FP to fabricate foams of controllable densities.

# CHAPTER 5

# FUTURE OPPORTUNITIES

## 5.1 The Effect of Molecular Weight on the Structural Recovery and Sintering Behavior of PTFE

Future opportunities for the scope of this work include optimizing the TMA parameters such that repeatable, sample representative data can be acquired for both the height ratio and modulus simultaneously. Successful interpretation of the storage and loss modulus results allow for more information to be garnered in terms of porosity reduction and entanglement formation during the observed transitions of the sintering profile. This may involve using data acquisition software with a load cell to manually measure the load such that modulus can be calculated in a more convenient and accurate fashion. This also allows for studying the load-deflection curves which can provide information regarding reversible versus irreversible changes pertaining to particle rearrangement.

To study the recovery behavior more closely, temperature dependent X-Ray measurements can be performed on cross sections of green PTFE billets using a similar sintering profile as done in TMA. By measuring spectra at various stages, one can then quantify the orientation parameter to assess the degree of anisotropy, which may depend on preform pressure, molecular weight, etc. In supplement, polarized optical microscopy measurements in transmission can be done in the melt to observe any preserved birefringence that may be indicative of the stored memory in PTFE crystals. This can then demonstrate a more fundamental understanding of the interesting melt dynamics of PTFE.

Additionally, SEM images of billets that have been quenched at various stages during the sintering process can provide information regarding morphological progression of particles.

Another challenge to investigate are property gradients that may be present due to inconsistent thermal history in large commercial billets. For example, one can cut pieces at various radii and perform screening studies (thermal analysis, optical microscopy, SEM, etc.), measuring any features that may be present due to deformities introduced from unoptimized process parameters. It is also commercially relevant to measure mechanical properties of skived films that are created from larger billets which are commonly sold to customers.

For SLS 3D printing powders, one strategy to enhance sintering efficacy is to generate kinetically trapped blends from two immiscible polymers using the same process as the grafting chemistry introduced in Chapter 2. For example, polymerizing styrene in the amorphous regions of polyolefins would generate immiscible blends rather than graft copolymers due to the low graft yield. This can enhance sintering of polyolefin powders as chain diffusion would be driven by the phase separation of the blend in addition to melting of the crystals. The same strategies used to characterize PTFE billets can be used to study SLS powders with some modification. For example, imposing radial confinement by placing the powder in a Tzero pan, and using a Tzero lid to distribute the load from the probe will allow for measurements during melting *in-situ* (Figure 58), which was not needed for PTFE billets due to the high melt viscosity.

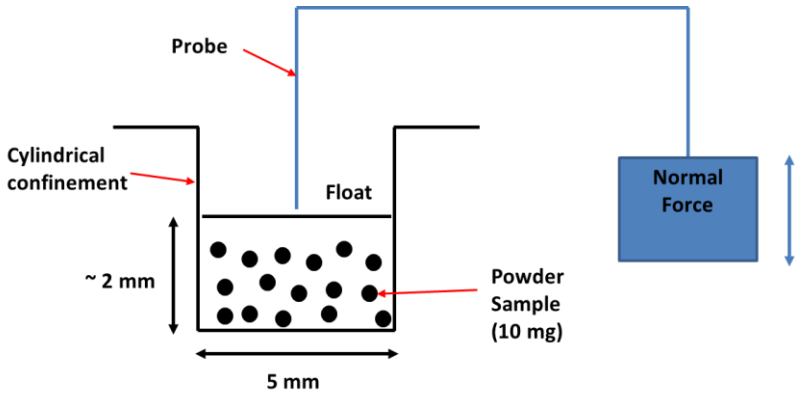


**Figure 58:** TMA setup for radial confinement of powders.

## 5.2 Upcycling by Grafting onto Semi-Crystalline Polymers using Supercritical $CO_2$

Morphological features of the graft copolymers created in Chapter 3 would be interesting to investigate. This includes SEM imaging of stained specimens such that the arrangement of the PS domains can be observed. How they organize around the crystalline regions will provide information regarding the properties these polymers may exhibit. If enough purified specimens can be created, mechanical testing should be performed in conjunction with these studies to elucidate mechanisms of yielding, failure, etc. It would also be enticing to study these copolymers as impact modifiers or compatibilizers by melt blending them with homopolymeric mixtures. One can then study morphological domains via SEM or X-Ray scattering as well as test for any mechanical improvement that may be provided from new energy dissipation mechanisms.

Additional grafting monomers can be used to further tune properties of semi-crystalline base polymers. As was discussed in Chapter 3, hydrophobicity and

hydrophilicity can be introduced to polyamides by changing the grafting monomer. It may also be interesting to use monomers whose polymers demonstrate low glass transition temperatures, creating a rubber or thermoplastic elastomer.

### 5.3 Evaluation of Adhesion Mechanisms in Frontally Polymerizable Adhesives

Fractographic analyses of mechanically tested lap shear specimens can be performed to elucidate the adhesion mechanisms more closely. In addition, changing the initiation site relative to the substrate and investigating how failure is affected will also provide insight regarding how heat generated from the front influences adhesion. Selective solvents can be used to dissolve certain substrates away from the adhesive, followed by characterizing the remaining surface using FTIR. This can determine whether the adhesive covalently bonds to polymers during FP. Cross section EDX can be performed on cut lap shear specimens to uncover whether there is special dependence on composition at distances from the interface. This can provide a metric for any local mixing between the adhesive and substrates which exhibit low glass transition or melt temperatures relative to the propagating front. Examining the metal wires after pull-out testing can also provide information about whether cure shrinkage or other factors play a role in adhesion to metals.

The volatiles produced during FP provide opportunities to generate foams. Nucleating and blowing agents can be added to formulations to create microcellular structures. Additionally, gelled formulations can be produced such that confinement is no longer needed before FP. Foams will then be formed in the presence of a crosslinked solid, where interesting morphology is produced as a consequence of fracture rather than off-

gassing into spherical cavities from a liquid. Microscopy can then be used to study the effect of formulation changes on the foam morphology.

## BIBLIOGRAPHY


1. Gamboni, O., Riul, C., Schmitt, N. & Canto, R. B. On the formation of defects induced by air trapping during cold pressing of PTFE powder Ot a. *Polymer (Guildf).* **82**, 75–86 (2016).

2. Fiocco, V., Caldeira, C., Bresciani, L. & Bresciani, R. Influence of Surface Crystalline Structures on DSC Analysis of PTFE. *Mater. Res.* **20**, 1350–1359 (2017).

3. Tomkovic, T. Rheology and processing of polytetrafluoroethylene ( PTFE ) paste. *Can. J. Chem. Eng.* 1852–1865 (2020) doi:10.1002/cjce.23816.

4. Gao, J., Ni, Z. & Liu, Y. The investigation of the structural change and the wetting behavior of electron beam irradiated PTFE film. *e-Polymers* **16**, 111–115 (2016).

5. Choi, K. & Spruiell, J. E. Structure Development in Multistage Stretching of PTFE Films. *J. Polym. Sci. Part B Polym. Phys.* **48**, 2248–2256 (2010).

6. Guenoun, G., Faou, J., Régnier, G., Schmitt, N. & Roux, S. Thermal cycling of cold-pressed PTFE compacts : Reversible and irreversible behavior. *Polym. Test.* **75**, 99–106 (2019).

7. Ganguly, R. & Lesser, A. J. Mechanism and kinetics of ultra-high molecular weight polytetrafluoroethylene sintering. *J. Appl. Polym. Sci.* **131**, 1–7 (2014).

8. Ebnesajjad, S. *Fluoroplastics, Volume 1: Non-Melt Processible Fluoroplastics*. (William Andrew, 2000).

9. Canto, R. B., Schmitt, N. & Carvalho, J. De. Experimental Identification of the Deformation Mechanisms During Sintering of Cold Compacted Polytetrafluoroethylene Powders. *Polym. Eng. Sci.* 2221–2235 (2011) doi:10.1002/pen.

10. Frenkel, J. Viscous Flow of Crystalline Bodies under the Action of Surface Tension. *J. Physics, USSR* **5**, 385–391 (1945).

11. Ristić, M. M. & Milosević, S. D. Frenkel's Theory of Sintering. *Sci. Sinter.* **38**, 7–11 (2006).

12. Bellehumeur, C. T., Kontopoulou, M. & Vlachopoulos, J. The role of viscoelasticity in polymer sintering. *Rheol. Acta* **37**, 270–278 (1998).

13. Ganguly, R. Process-Structure-Property Relationship in Ultra High Molecular Weight Polytetrafluoroethylene and. (2015).

14. Drummer, D., Greiner, S., Zhao, M. & Wudy, K. A novel approach for understanding laser sintering of polymers. *Addit. Manuf.* **27**, 379–388 (2019).

15. Pereira, T., Kennedy, J. V. & Potgieter, J. A comparison of traditional manufacturing vs additive manufacturing, the best method for the job. *Procedia Manuf.* **30**, 11–18 (2019).

16. Goodridge, R. D., Tuck, C. J. & Hague, R. J. M. Laser sintering of polyamides and other polymers. *Prog. Mater. Sci.* **57**, 229–267 (2012).

17. Schmid, M., Amado, A. & Wegener, K. Polymer powders for selective laser sintering (SLS). *AIP Conf. Proc.* **1664**, (2015).

18. Negrov, D. A. & Eremin, E. N. Structuring peculiarities of polytetrafluoroethylene modified with boron nitride when activated with ultrasonic exposure. *Procedia Eng.* **152**, 570–575 (2016).

19. Starkweather, H. W. & Jones, G. A. The Heat of Fusion of Polytetrafluoroethylene. *J. Polym. Sci. Polym. Phys. Ed.* **20**, 751–761 (1982).

20. Guenoun, G., Faou, J., Régnier, G., Schmitt, N. & Roux, S. PTFE crystallization mechanisms : Insight from calorimetric and dilatometric experiments. *Polymer (Guildf).* **193**, 122333 (2020).

21. Blaine, R. L. Thermal Applications Note - Polymer Heats of Fusion. *Therm. Appl. Note* (2002).

22. Patlazhan, S. & Remond, Y. Structural mechanics of semicrystalline polymers prior to the yield point: A review. *J. Mater. Sci.* **47**, 6749–6767 (2012).

23. Rahimi, A. R. & Garciá, J. M. Chemical recycling of waste plastics for new materials production. *Nat. Rev. Chem.* **1**, (2017).

24. Plastic upcycling. *Nat. Catal.* **2**, 945–946 (2019).

25. Garcia, J. M. & Robertson, M. L. The future of plastics recycling. *Science (80-. ).* **358**, 870–872 (2017).

26. Pan, D. *et al.* Research progress on catalytic pyrolysis and reuse of waste plastics and petroleum sludge. *ES Mater. Manuf.* 3–15 (2021) doi:10.30919/esmm5f415.

27. Pan, D., Su, F., Liu, C. & Guo, Z. Research progress for plastic waste management and manufacture of value-added products. *Adv. Compos. Hybrid Mater.* **3**, 443–461 (2020).

28. Koning, C., Van Duin, M., Pagnoulle, C. & Jerome, R. Strategies for compatibilization of polymer blends. *Prog. Polym. Sci.* **23**, 707–757 (1998).

29. Galloway, J. A., Jeon, H. K., Bell, J. R. & MacOsko, C. W. Block copolymer compatibilization of cocontinuous polymer blends. *Polymer (Guildf).* **46**, 183–191 (2005).

30. Zhou, Y., Wang, P., Ruan, G., Xu, P. & Ding, Y. Synergistic Effect of P[MPEGMA-IL] Modified Graphene on Morphology and Dielectric Properties of PLA/PCL Blends. *ES Mater. Manuf.* 20–29 (2020) doi:10.30919/esmm5f928.

31. Zou, W., Huang, J., Zeng, W. & Lu, X. Effect of Ethylene–Butylacrylate–Glycidyl Methacrylate on Compatibility Properties of Poly (butylene terephthalate)/ Thermoplastic Polyurethane Blends. *ES Energy Environ.* 67–73 (2020) doi:10.30919/esee8c180.

32. Li, Z., Ma, J., Cheng, C., Zhang, K. & Wooley, K. L. Synthesis of hetero-grafted amphiphilic diblock molecular brushes and their self-assembly in aqueous Medium. *Macromolecules* **43**, 1182–1184 (2010).

33. Feng, H., Lu, X., Wang, W., Kang, N. G. & Mays, J. W. Block copolymers: Synthesis, self-assembly, and applications. *Polymers (Basel).* **9**, (2017).

34. Abreu, F. O. M. S., Forte, M. M. C. & Liberman, S. A. SBS and SEBS block copolymers as impact modifiers for polypropylene compounds. *J. Appl. Polym. Sci.* **95**, 254–263 (2005).

35. Feng, C. *et al.* Well-defined graft copolymers: From controlled synthesis to multipurpose applications. *Chem. Soc. Rev.* **40**, 1282–1295 (2011).

36. Verduzco, R., Li, X., Pesek, S. L. & Stein, G. E. Structure, function, self-assembly, and applications of bottlebrush copolymers. *Chem. Soc. Rev.* **44**, 2405–2420 (2015).

37. Sihvonen, M., Järvenpää, E., Hietaniemi, V. & Huopalahti, R. Advances in supercritical carbon dioxide technologies. *Trends Food Sci. Technol.* **10**, 217–222 (1999).

38. Kung, E., Lesser, A. J. & McCarthy, T. J. Morphology and mechanical performance of polystyrene/polyethylene composites prepared in supercritical carbon dioxide. *Macromolecules* **31**, 4160–4169 (1998).

39. Wissinger, R. G. & Paulaitis, M. E. Mixtures at Elevated Pressures. **25**, 2497–2510 (1987).

40. Berens, A. R., Huvard, G. S., Korsmeyer, R. W. & Kunig, F. W. Application of compressed carbon dioxide in the incorporation of additives into polymers. *J. Appl. Polym. Sci.* **46**, 231–242 (1992).

41. Kendall, J. L., Canelas, D. A., Young, J. L., Desimone, J. M. & Coupling, C. O. Polymerizations in Supercritical Carbon Dioxide. 9–12 (2000) doi:10.1021/cr9700336.

42. Zhou, Y. *et al.* Recent Advances in Organic/Composite Phase Change Materials for Energy Storage. *ES Energy Environ.* **c**, 28–40 (2020).

43. Lu, X. *et al.* Polyethylene Glycol/Carbon Black Shape-Stable Phase Change Composites for Peak Load Regulating of Electric Power System and Corresponding Thermal Energy Storage. *Eng. Sci.* 25–34 (2020) doi:10.30919/es8d901.

44. Zhou, Y. *et al.* Recent Advances in Thermal Interface Materials. *ES Mater. Manuf.* **33**, 8–11 (2020).

45. Li, T. *et al.* Achieving Better Greenhouse Effect than Glass: Visibly Transparent and Low Emissivity Metal-Polymer Hybrid Metamaterials. *ES Energy Environ.* (2019) doi:10.30919/esee8c325.

46. Sun, L. *et al.* Optimizing Strategy for the Dielectric Performance of Topological-structured Polymer Nanocomposites by Rationally Tailoring the Spatial Distribution of Nanofillers. *Eng. Sci.* 95–105 (2020) doi:10.30919/es8d1148.

47. Chen, J., Zhu, Y., Guo, Z. & Nasibulin, A. G. Recent Progress on Thermo-electrical Properties of Conductive Polymer Composites and Their Application in Temperature Sensors. *Eng. Sci.* 13–22 (2020) doi:10.30919/es8d1129.

48. Jing, X., Wei, J., Liu, Y., Song, B. & Liu, Y. Deployment Analysis of Aramid Fiber Reinforced Shape-Memory Epoxy Resin Composites. *Eng. Sci.* 44–53 (2020) doi:10.30919/es8d1120.

49. Zhang, D., Sun, J., Lee, L. J. & Castro, J. M. Overview of Ultrasonic Assisted Manufacturing Multifunctional Carbon Nanotube Nanopaper Based Polymer Nanocomposites. *Eng. Sci.* 35–50 (2020) doi:10.30919/es5e1002.

50. Yan, X. *et al.* Efficient Solvent-Free Microwave Irradiation Synthesis of Highly Conductive Polypropylene Nanocomposites with Lowly Loaded Carbon Nanotubes. *ES Mater. Manuf.* 21–33 (2020) doi:10.30919/esmm5f716.

51. Nayak, P. L. Grafting of Vinyl Monomers onto Nylon. *J. Macromol. Sci. Part C* **17**, 267–296 (1979).

52. Mukherjee, A. K. & Coel, H. R. Modification of Nylons via Graft Copolymerization. *J. Macromol. Sci. Part C* **25**, 99–117 (1985).

53. El-Rafie, M. H., Khalil, M. I. & Hebeish, A. Azobisisobutyronitrile-induced vinyl graft polymerization onto nylon 66. **19**, 1677–1684 (1975).

54. Langer, N. M. & Wilkie, C. A. Surface modification of polyamide-6: Graft copolymerization of vinyl monomers onto polyamide-6 and thermal analysis of the graft copolymers. *Polym. Adv. Technol.* **9**, 290–296 (1998).

55. Belfer, S., Purinson, Y., Fainshtein, R., Radchenko, Y. & Kedem, O. Surface modification of commercial composite polyamide reverse osmosis membranes. *J. Memb. Sci.* **139**, 175–181 (1998).

56. Coltelli, M. B., Angiuli, M., Passaglia, E., Castelvetro, V. & Ciardelli, F. Formation of short and long chain branches during the free radical functionalization of polyamide 6 in the melt. *Macromolecules* **39**, 2153–2161 (2006).

57. Dong, Q. & Liu, Y. Styrene-assisted free-radical graft copolymerization of maleic anhydride onto polypropylene in supercritical carbon dioxide. *J. Appl. Polym. Sci.* **90**, 853–860 (2003).

58. Lee, S., Soonjong, K. & Azzam, F. The University of Akron. (1997).

59. Polymer Properties Database. *crow* https://polymerdatabase.com/polymer physics/SolubilityParameter.html (2015).

60. Kumosa, L., Armentrout, D., Benedikt, B. & Kumosa, M. An investigation of moisture and leakage currents in GRP composite hollow cylinders. *IEEE Trans. Dielectr. Electr. Insul.* **12**, 1043–1059 (2005).

61. Odian, G. *Principles of Polymerization*. *Principles of Polymerization* (2004). doi:10.1002/047147875x.

62. Dashairya, L., Sahu, A. & Saha, P. Stearic acid treated polypyrrole-encapsulated melamine formaldehyde superhydrophobic sponge for oil recovery. *Adv. Compos. Hybrid Mater.* **2**, 70–82 (2019).

63. Lutz, J. F. Polymerization of oligo(ethylene glycol) (meth)acrylates: Toward new generations of smart biocompatible materials. *J. Polym. Sci. Part A Polym. Chem.* **46**, 3459–3470 (2008).

64. Pojman, J. A. *Frontal Polymerization*. *Polymer Science: A Comprehensive Reference, 10 Volume Set* vol. 4 (Elsevier B.V., 2012).

65. Pojman, J. A., Ilyashenko, V. M. & Khan, A. M. Reaction Waves. **92**, 2825–2837 (1996).

66. Ivanov, V. V. & Decker, C. Kinetic study of photoinitated frontal polymerization. *Polym. Int.* **50**, 113–118 (2001).

67. Norrish, R. G. W. & Smith, R. R. Catalysed Polymerization of Methyl Methacrylate in the Liquid Phase. *Nature* **150**, 336–337 (1942).

68. Fiori, S., Mariani, A., Ricco, L. & Russo, S. First synthesis of a polyurethane by frontal polymerization. *Macromolecules* **36**, 2674–2679 (2003).

69. Begishev, V. P., Vol'pert, V. A., Davtyan, S. P. & Malkin, A. Y. . *Dokl. Akad. Nauk SSSR* **279**, 909–912 (1984).

70. Bomze, D., Knaack, P. & Liska, R. Successful radical induced cationic frontal polymerization of epoxy-based monomers by C-C labile compounds. *Polym. Chem.* **6**, 8161–8167 (2015).

71. Liska, R., Binzem, D. & Kern, W. Method for Frontal Polymerization of Cationically Polymerizable Monomers. (2017).

72. Pham, H. Q. & Marks, M. J. . *Epoxy Resins, Ullmann's Encyclopedia of Industrial Chemistry* (2005).

73. Crivello, J. V. Hybrid free radical/cationic frontal photopolymerizations. *J. Polym. Sci. Part A Polym. Chem.* (2007) doi:10.1002/pola.22177.

74. Vitale, A., Sangermano, M., Bongiovanni, R., Burtscher, P. & Moszner, N. Visible light curable restorative composites for dental applications based on epoxy monomer. *Materials (Basel).* (2014) doi:10.3390/ma7010554.

75. Lesser, A. J. & Lampe, M. J. Polymerizing Composition, Method of Manufacture Thereof and Articles Comprising the Same. (2018).

76. Knaack, P., Klikovits, N., Tran, A. D., Bomze, D. & Liska, R. Radical induced cationic frontal polymerization in thin layers. *J. Polym. Sci. Part A Polym. Chem.* **57**, 1155–1159 (2019).

77. Holt, T. Von, Fazende, K., Jee, E., Wu, Q. & Pojman, J. A. Cure-on-demand wood adhesive based on the frontal polymerization of acrylates. *J. Appl. Polym. Sci.* **133**, 5–9 (2016).

78. Wigdorski 2016, Reactive Film Adhesive, US Patent 9512340.

79. Pfeil, I. A., Morbidelli, M., Buergel, T. & Rosell, A. Long pot life mortar acting by rapid frontal polymerisation is used e . g . for xing metal rods in concrete and comprises polymerizable monomers and / or hardenable resins with heat-activated initiators or accelerators DE10002367C1. 1–8 (2019).

80. Volkersen, O. Die Nietkraftverteilung in zugbeanspruchten \mbox{Nietverbindungen} mit konstanten Laschenquerschnitten. *Luftfahrtforschung* (1938).

81. Spiegel, S. Recent advances in applied polymer science. *J. Appl. Polym. Sci.* **135**, (2018).

82. Engineering ToolBox. *Thermal Conductivity of some selected Materials and Gases* https://www.engineeringtoolbox.com/thermal-conductivity-d_429.html (2003).